


1-1-2018

# Uncertainty In Combustion Reaction Rates And Its Effects On Combustion Simulations

Joshua Piehl  
*Wayne State University,*

Follow this and additional works at: [https://digitalcommons.wayne.edu/oa\\_theses](https://digitalcommons.wayne.edu/oa_theses)

 Part of the [Chemistry Commons](#), and the [Mechanical Engineering Commons](#)

---

## Recommended Citation

Piehl, Joshua, "Uncertainty In Combustion Reaction Rates And Its Effects On Combustion Simulations" (2018). *Wayne State University Theses*. 639.

[https://digitalcommons.wayne.edu/oa\\_theses/639](https://digitalcommons.wayne.edu/oa_theses/639)

This Open Access Thesis is brought to you for free and open access by DigitalCommons@WayneState. It has been accepted for inclusion in Wayne State University Theses by an authorized administrator of DigitalCommons@WayneState.

**UNCERTAINTY IN COMBUSTION REACTION RATES AND ITS EFFECTS ON  
COMBUSTION SIMULATIONS**

by

**JOSHUA A. PIEHL**

**THESIS**

Submitted to the Graduate School

of Wayne State University

Detroit, Michigan

in partial fulfillment of the requirements

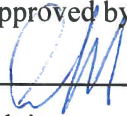
For the degree of

**MASTER OF SCIENCE**

2018

MAJOR: MECHANICAL ENGINEERING

Approved by:

 Omid Samimi-Abianeh 6/21/2018

Advisor

Date

**© COPYRIGHT BY  
JOSHUA A. PIEHL  
2018  
All Rights Reserved**

## **DEDICATION**

To my family and friends, whose constant support has allowed me to reach this far.

## ACKNOWLEDGEMENTS

Foremost, I would like to thank my advisor Dr. Omid Samimi-Abianeh for his constant support and mentoring. With his mentorship, I have learned a great deal about combustion physics and research during my time in the Combustion Physics Laboratory. His support has allowed me to grow as a researcher and as an individual. I would also like to thank Dr. Luis Bravo from the Army Research Laboratory for his support and mentorship in this project. He provided invaluable feedback that improved my understanding of the fundamental physics that occur during the simulations. I want to express my sincere appreciation to my committee members, Dr. Naeim Henein and Dr. Marcis Jansons, for supporting me during this project. I would like thank the Department of Defense High Performance Computing Modernization Program (HPCMP) for providing me computational time on the DoD's supercomputer Excalibur. It was a great privilege to use the cluster. Finally, I would like to thank my friends and family that have provided me the support to continue my education.

## TABLE OF CONTENTS

DEDICATION.....	ii
ACKNOWLEDGEMENTS.....	iii
LIST OF FIGURES .....	vii
LIST OF TABLES.....	viii
CHAPTER 1 .....	1
1    INTRODUCTION .....	1
CHAPTER 2 .....	3
2    LITERATURE REVIEW .....	3
2.1    CHAPTER OVERVIEW.....	3
2.2    EXPERIMENTAL DATA REVIEW.....	3
2.2.1    SPRAY PENETRATION .....	3
2.2.2    COMBUSTION CHARACTERISTICS.....	5
2.2.3    MIXING MEASUREMENTS .....	7
2.2.4    NOZZLE GEOMETRY AND FLOW CHARACTERISTICS.....	8
2.3    NUMERICAL SIMULATION REVIEW .....	9
2.3.1    FUEL SPRAYS.....	9
2.3.2    COMBUSTION CHARACTERISTICS.....	10
2.3.3    TURBULENCE MODELLING EFFECTS .....	11
CHAPTER 3 .....	13

3	COMPUTATIONAL METHODOLOGY .....	13
3.1	CHAPTER OVERVIEW .....	13
3.2	SENSITIVITY ANALYSIS METHODOLOGY .....	13
3.3	0-D COMPUTATION METHODOLOGY .....	14
3.3.1	GOVERNING EQUATIONS .....	14
3.3.2	COMBUSTION MODELING .....	15
3.4	3-D COMPUTATIONAL METHODOLOGY .....	17
3.4.1	GEOMETRY AND MESH GENERATION .....	17
3.4.2	SPRAY MODELING.....	20
3.4.3	DROPLET COLLISION MODELING .....	23
3.4.4	DROPLET EVAPORATION MODELING .....	28
3.4.5	TURBULENCE MODELING .....	29
3.4.6	COMBUSTION MODELING .....	31
	CHAPTER 4 .....	32
4	RESULTS AND DISCUSSION .....	32
4.1	CHAPTER OVERVIEW .....	32
4.2	SENSITIVITY ANALYSIS .....	32
4.3	0-D AND 3-D COMBUSTION SIMULATIONS.....	35
	CHAPTER 5 .....	45
5	CONCLUSION.....	45

REFERENCES ..... 49

ABSTRACT..... 56



## LIST OF FIGURES

FIGURE 1.1 Experimental shock tube ignition delay data and various kinetic mechanisms (left) and experimental spray combustion data with the same kinetic mechanisms used to predict the ignition delay (right) [1].....	2
FIGURE 3.1 The 3D computational geometry used for this work.....	17
FIGURE 3.2 Gas temperature in the combustion chamber using different maximum cell count thresholds. The vertical lines show at which point in the simulation the maximum cell count was achieved [37].....	19
FIGURE 3.3 Mesh used for all 3-d cases in the simulation. Mesh size was determined in [37].....	19
FIGURE 3.4 Visualization of blob-injection model of reitz [40].....	20
FIGURE 3.5 Depiction of the KH-RT breakup length model. Prior to length $l_b$ , the Kelvin-Helmholtz instabilities only impact the breakup of the spray. After this length, the Rayleigh-Taylor instabilities also impact the spray breakup [43].....	22
FIGURE 3.6 Figure of droplet-droplet collision. This depiction shows how converge calculates the post-collision direction and velocity of the droplets as outlined in the above equations. Image adopted from [46] with permission.....	26
FIGURE 4.1 Simulations and experimental ignition delay at an equivalence ration of 1. N-dodecane is the fuel used in this study.....	33
FIGURE 4.2 Simulations and experimental ignition delay at an equivalence ration of 2. N-dodecane is the fuel used in this study.....	33
FIGURE 4.3 Mass history of key species in the combustion chamber. Initial ambient gas temperature was 1000 K. The ignition delay predicted by the species history is shown in red. As a comparison, the pressure-based ignition delay is shown as well. The luminosity-based ignition delay timing and its respective uncertainty is shown by the gray box. This figure is adopted from [23] with permission.....	37
FIGURE 4.4 Comparison of the temperature contours of the different mechanisms compared to the baseline mechanism. These contours were visualized 0.285 ms after the start of injection at an initial gas temperature of 1000 K.....	40
FIGURE 4.5 Ignition delays of the turbulent spray simulations using the different mechanisms compared to experimental data [1].....	40
FIGURE 4.6 Liquid and vapor penetration lengths of the various mechanisms at an ambient temperature of 900 K.....	42
FIGURE 4.7 Flame lift-off lengths for each mechanism compared to experimental data of [1].....	44

## LIST OF TABLES

TABLE 4.1 Critical reactions.....	34
TABLE 4.2 A summary of initial conditions used for the simulations.....	35
TABLE 4.3 Ignition delays of mechanisms with modified reaction rates. Note how the 0-D predictions do not line up with the 3-D predictions.....	39

## Chapter 1

### 1 Introduction

As time progresses, the battle to impede climate change has grown more fierce. Combustion research has become paramount to impeding the progress of climate change whilst maintaining the standard of living that citizens of the first-world are expecting. Researchers have made great strides in understanding the intricacies of combustion through experimentation. Such experimentation is augmented by simulations that use high-performance computing to better understand how fuel disperses and which reaction pathways are critical to combustion. Experimental data has led to the development of chemical kinetic models that can simulate combustion processes to a seemingly high degree of accuracy. When compared to quasi-steady state experimental data of ignition delay tests (e.g. tests performed using a batch reactor, shock tube, or Rapid Compression Machine (RCM)), these computational models seem to accurately predict the ignition delay of a multitude of fuels at a range of conditions.

However, when these models are coupled with a 3-D computational fluid dynamics (CFD) program to predict turbulent spray combustion, the predicted results of the simulations do not match with the results recorded during experimentation. This is well demonstrated in the combustion test results of the Engine Combustion Network (ECN) [1]. This international research collaboration has well-defined initial conditions for experiments, which created a vast library of experimental data that can be used for kinetic mechanism validation. Figure 1 is a compilation of ignition delay data for both experiments and simulations. As it is shown, mechanisms that agree with the 0-D data (i.e. experiments that run at quasi-steady state conditions) do not predict the turbulent spray combustion well. The same goes for mechanisms that were verified by spray combustion experimentation. This begs the question, if the underlying chemical reactions are the

same for both cases, what causes the discrepancy between the predicted ignition delays of the 0-D and 3-D simulations?

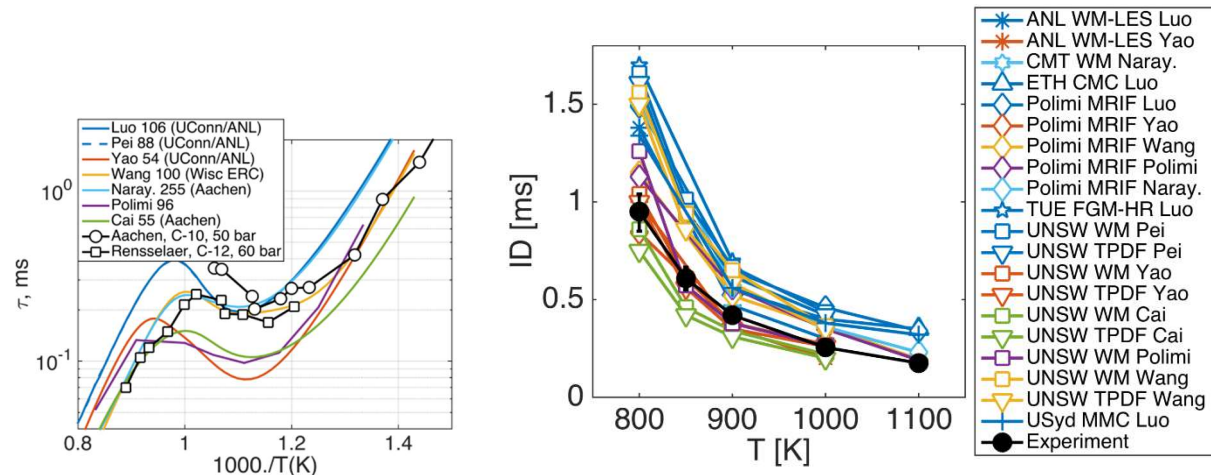


**Figure 1.1 Experimental shock tube ignition delay data and various kinetic mechanisms (left) and experimental spray combustion data with the same kinetic mechanisms used to predict the ignition delay (right) [1].**

The goal of this study is to understand the uncertainty in a chemical reaction's rate and how it impacts the spray combustion. To achieve this goal, a well-validated detailed chemical mechanism of n-dodecane has been reduced to analyze the reactions effects on combustion. The most critical of these reactions have been identified through a sensitivity analysis and then independently subjected to ignition delay tests in 0-D and 3-D environments to study their effects on combustion. The results of this study are presented herein and recommendations for future work are provided.

Following this introduction, a literary review of the experimental tests and CFD results will be discussed. After that, the numerical methodology will be described, after which the results will be presented.

## CHAPTER 2

### 2 LITERATURE REVIEW

#### 2.1 Chapter Overview

This section is divided into two different parts: experimental results and CFD simulations. The experimental results will look into the work done in spray penetration measurements, flame lift-off length (LOL) measurements, ignition delay measurements, mixing measurements, internal nozzle geometry flow, and nozzle geometry effects. The CFD section will looking into the modeling of mono- and multi-component fuel sprays, flame LOL measurements, auto-ignition simulations, and various turbulence modeling simulations.

#### 2.2 Experimental Data Review

This section reviews the experiments performed to evaluate combustion from turbulent sprays. It reviews the spray penetration measurements, ignition delay calculations, flame lift-off length distances, fuel and air mixing, and injector nozzle geometry.

##### 2.2.1 Spray Penetration

There has been much work investigating spray penetration lengths and the effect of different parameters on the spray. The experimental research has investigated the effect of the ambient density and temperature, injection pressure, nozzle orifice diameter and aspect ratio, fuel temperature and fuel volatility on fuel sprays [2-6]. Additional experiments have investigated the physics of the jet ligaments and droplets formed under various conditions [7]. These experiments were performed in constant volume combustion chambers with optical accesses similar in size and shape of the one used in [1]. The experiments used a variety of different visualization methods to observe the spray, such as: schlieren imaging [2-6], high-speed Mie-Scatter [3-6], and high-speed long-distance microscopic imaging [7]. These imaging techniques are usually coupled together as the combined data can show spray features that are obscured by combustion [4]. In a later study,

Pickett et al. [6] demonstrated that how these imaging techniques are captured and analyzed can produce uncertainty in the results and thus caution must be taken when performing the experiments.

These experiments have been insightful into the physics of liquid jets. It has been shown that an increase in the ambient gas density and temperature shortens the liquid penetration length [2,3,5]. The ambient density was shown to increase the spray dispersion and slow the jet penetration velocity. Pickett et al. [5] investigated conditions that were similar to those found in diesel engines approaching top dead center. They reported that a volume reduction associated with 15 crank angle degrees reduced the liquid penetration length by approximately a factor of 2. While both factors have been shown to heavily impact the liquid length, the effect created by the ambient gas density was the greatest [3].

In addition, the results show that nozzle orifice diameter plays a critical role in determining the liquid penetration length. Siebers [3] showed that the liquid length of the jet was linearly dependent on the size of the nozzle orifice; however, this trend is independent of all other factors. This was later confirmed by Pickett et al. [5], who noted that the maximum penetration length of the spray can be the same as those nozzles with larger orifices if the injected mass is to be held constant (i.e. the injection duration is longer). Furthermore, they noted that short injection durations with high injection pressures produce the same maximum penetration length as injection events that were longer with lower injection pressures. Pickett et al. continued to say that multiple injection events, normally reducing the liquid penetration length, can produce the same liquid penetration length as its single injection counterparts [5]. Despite the great impact on the spray by the nozzle orifice, the nozzle orifice aspect ratio has an inconsistent effect on the spray [3].

Fuel properties were shown to impact the liquid penetration length [3,5]. Siebers showed that as the fuel temperature increased, the liquid length decreased. This was correlated to a 12% decrease in the length of the spray for a 60 K increase in temperature [3]. In addition, the study found that lower fuel volatility resulted in a longer liquid penetration length. In a multicomponent fuel spray, it is the component with the lower volatility that determines the liquid penetration length [5]. However, Siebers noted that the importance of volatilities on the liquid penetration length decreases as ambient temperature increases, as the penetration lengths appear to converge at higher ambient temperatures for different fuels [3].

Manin et al., analyzed the liquid break-up in closer detail using long-distance microscopy visualization techniques. In their work, the effects of droplet surface tension contributing to the break-up at low temperatures was captured. They confirmed that droplet break-up increased as the ambient gas density increased due to greater drag forces on the droplet [7]. However, when the pressures increased to those of engine applications, the effect of surface tension is less apparent (even indiscernible).

As a way to model all these parameters, Siebers developed a scaling law for the liquid penetration length [8]. This scaling law took into consideration ambient temperature, ambient density, fuel volatility, fuel temperature, and nozzle orifice size.

### **2.2.2 Combustion Characteristics**

Traditionally, diesel spray combustion has two characteristics that are quantified during experimentation: flame lift-off length (LOL) and ignition delay of the fuel. More emphasis has been placed on LOL in the experiments involving turbulent spray combustion. As in the previous section, the experiments discussed in this section have been performed using a constant volume combustion chamber with optical accesses to measure the combustion processes using different

visualization techniques. In these experiments, it was confirmed numerous times that ignition delay and LOL have an inverse relationship with ambient temperature and pressure [9-13]. In addition to the relationship with ambient conditions, many observations have been made about diesel spray combustion. Higgins et al. used pressure trace measurements and chemiluminescence imaging to confirm the two-stage ignition delay behavior found in diesel combustion at a range of different temperatures and pressures [9]. The conditions used were similar to those found in medium- and heavy-duty diesel engines. Higgins and Siebers continued studying LOL using OH chemiluminescence in [10]. Their work concluded that chemical luminescence intensity does not vary with ambient temperature and pressure; as a result, the researchers concluded that the optimal wavelength to observe OH luminosity is at the 310 nm wavelength [10].

Further studies observed a cool flame forming in approximately the same location as the steady-state lift-off length prior to auto-ignition [11]. This is indicative of first stage ignition processes affecting the LOL and disputes the notion that flame propagation impacts the stabilized length of flame lift-off. Benajes et al. used Schlieren images to characterize the onset of these cool flames and developed a new method to predict when these flames would occur based on boundary conditions [12]. This methodology also improved quantification of the second stage ignition delay.

Continued quantification of the lift-off length has led researchers to study how initial conditions impact the LOL. Different fuels were tested to compare the physical properties of the fuel and how it impacts the lift-off length. It was determined that the ignition quality of the fuel directly impacts the LOL during combustion [11]. Additionally, the mixing of the oxidizer with the fuel impacts the LOL as described in [13]. This mixing process is determined by the atomization of the jet stream as will be discussed in a later section. However, it was found that increasing droplet velocity (through increased injection pressure) resulted in an increased LOL



[13]. Interestingly, the equivalence ratio at the location of the LOL remains consistent despite changes in the ambient conditions [13]. Overall, these observations are essential to modelling the combustion of the diesel spray effectively.

### **2.2.3 Mixing Measurements**

It is well-known that a proper balance of fuel and oxidizer must be mixed together to initiate combustion. Therefore, understanding how a pure liquid jet of fuel mixes in a combustion chamber is essential for a better comprehension of combustion. Since this knowledge is vital to diesel engine combustion modes, the work of Espey et al. used Rayleigh scattering techniques in an optically accessible diesel engine to study the mixing of fuel and air [14]. The researchers noted the initial fuel jet is dense and does not have much air entrained inside. However, as the jet propagates out, the air and fuel are uniformly mixed throughout the leading portion of the jet. This mixture is still fuel rich ( $\phi = 2-4$ ) but the equivalence ratio sharply drops in the front and sides of the jet. Interestingly, combustion of the mixture occurs simultaneously in these regions around the jet, leading to a fuel-rich combustion as opposed to a stoichiometric combustion as previously hypothesized [14].

Other studies have used Rayleigh scattering to provide further data about fuel and air mixing. In [15], Fielding et al. showed that depolarization Rayleigh scattering was a viable diagnostic tool for argon- and air-diluted mixtures. This was proven useful for mixtures that possess molecules that can significantly deviate the depolarization ratio from that of the oxidizer (e.g. methane) [15]. Later on Idicheria and Pickett explored the sources of error associated with the Rayleigh scattering imaging technique to improve the data gathered using this method [16]. Using a constant volume combustion chamber, they noted that careful placing the laser screen to avoid extraneous elastic scattering and correct for laser flare on the shot to shot variation would

lower the error significantly. Furthermore, a wavelength of 532 nm was recommended due to its great signal-to-noise ratio [16].

If Rayleigh scattering was not an option to visualize the mixing, Blessinger et al. showed that high-speed Schlieren and Mie-scattering imaging techniques are able to capture the mixing. In fact, these techniques are sensitive enough to capture areas of low equivalence ratio (i.e. regions on the edge of the spray) [17]. This sensitivity allows for vapor envelopes and probability curves to be drawn for the spray. When comparing the visual techniques, it was found that Rayleigh scattering showed more variability than Schlieren imaging [17]. Based on these results, it was recommended that modelers use the probability curves to validate their vapor penetration predictions.

#### **2.2.4 Nozzle Geometry and Flow Characteristics**

As mentioned in the spray parametrization section, the nozzle orifice has a significant impact on combustion during fuel injection. Further quantification of nozzle geometry has been performed to test its impact on the spray combustion. It was found that nozzle orifices are cylindrical or divergent in shape and can vary from the manufacturing design by up to 8% [18]. In addition, it was discovered that fuel injectors induce cavitation based on the mass flow and momentum flux measurements of [18]. Manufacturer variability, cavitation, orifice diameter, and injection pressure are shown to impact the spray [18,19]. A correlation between nozzle conditions and CH/OH radicals was observed [19]. CH radicals are influenced by the spray pattern, which then relates to OH radical production. Thus, it was discovered that nozzle geometry has a direct impact on the combustion progress via the CH and OH radical production.

## 2.3 Numerical Simulation Review

This section reviews the numerical simulations that have been performed to improve turbulent spray combustion. Similar to the experimental review, this section covers spray penetration measurements, ignition delay predictions, flame lift-off length simulations, and turbulence model effects on the combustion.

### 2.3.1 Fuel Sprays

The physics behind fuel spray and atomization are complex. Much research has been performed to improve the computational sub-models used to create fuel jets. Validation studies have been done to confirm the penetration lengths and mixture fractions of diesel sprays [20-23]. These studies used n-heptane [20,21] and n-dodecane [22] to mimic the physical properties of the fuel. These surrogates were shown to predict the physical spray properties accurately with the sub-models used in the study. Further analysis into the accuracy of the sub-models was done in [23]. This study compared the sub-model accuracy to the experimental data of [1]. The spray penetrations and fuel vapor mass fractions predictions were used to validate the CFD sub-models.

In addition to the macroscopic sub-models, microscopic effects of the spray were modelled. Droplet collision and coalescence models have been updated to include droplets of different densities [24]. This sub-model when coupled with other models had good agreement with experimental data for liquid and vapor penetration lengths at ambient densities of 20 and  $40 \frac{kg}{m^3}$ . This new model predicts smaller SMD for the droplets compared to the model of O'Rourke and Bracco. However, the prediction of spray penetration and mass-averaged velocity was in good agreement with the other model [24].

Evaporation models have been refined to improve the fuel mixing in simulations. Models for unsteady evaporation for mono-component and multi-component surrogates have been

developed to improve the accuracy of the CFD solver [25,26]. These models show that evaporation near the nozzle is difficult due to the liquid core of the jet and the time it takes for the droplets to breakup from the jet. The more volatile components evaporate quicker from the droplet than the less volatile components do [26]. This is reflective in the models as the light components are more upstream of the spray plume, while the heavier components are found more-so at the tip of the jet [25]. These models show accurate predictions of spray penetration when compared to experimental data.

### **2.3.2 Combustion Characteristics**

Reacting simulations provide further insight into the physics behind combustion. Much like the experimental data, the simulations are used for ignition delay validation [7,21,23,27,28] and lift-off length predictions [7,23,27-29]. These studies have revealed a wealth of information that benefits our understanding of combustion. It was demonstrated that ignition location in a spray is dependent on the spray atomization when compared to the OH\* chemiluminescence data [21]. Species histories have been used to demonstrate a more accurate way of calculating the ignition delay as demonstrated in [23]. Using the time histories of the hydroperoxyalkyl radicals to calculate the time of autoignition was demonstrated as a more accurate way to calculate ignition delay when compared with experimental data. The effect of ambient oxygen on the ignition delay has been tested as well and have shown good agreement with measured data [7,27,29]. Although these results are promising, these results still depend on the accuracy of the chemical mechanism [28].

Flame LOL is dependent on numerous factors and requires many factors to develop the flame. Flame structure has been shown to change with different realizations of numerical simulations [7,29]. Numerical investigations have been performed to better understand which

parameters are most critical for flame development. [29] studied LOL by correlating it to flamelet extinction. The study concluded that while flame stabilization in spray jets is effected by flamelet extinction, it is insufficient to say that flame stabilization the only parameter that affects the flame LOL [29]. During the process of flame propagation, it was observed that a developing flame moves in both directions of the spray. The flame propagates faster downstream than it does upstream until the flame stabilizes [27]. Coupled with this finding, [27] showed the results for the same model are similar when using two different CFD models. There were some minor differences in predicted LOL, flame shape, and flame penetration; nevertheless, both solvers were able to predict the experimental data quite nicely [27].

### **2.3.3 Turbulence Modelling Effects**

Two turbulence models are mostly used for modelling spray combustion: RANS and LES. LES is known to resolve the large eddies that RANS models at the expense of more computational time. Studies have been performed to see if the increased accuracy of the LES model is worth the additional computational expense when simulating turbulent spray combustion.

It was found that liquid and vapor penetration lengths and flame lift-off lengths are captured well by both models when compared to experimental data [30]. However, the intricacies of the spray combustion are better captured by the LES turbulence model. Since LES resolves the large eddies, it is able to predict the complex distribution of equivalence ratio and soot contours quite well, whereas the RANS models predict a layer of equivalence ratios and soot contours from the spray jet [28,30,31]. The complex flow field allows the LES model to have an asymmetric fuel spray as opposed to the symmetric jet created in the RANS model [31]. In addition, LES shows a more realistic flame development compared to the RANS model. The flames in LES propagate from the source of ignition and more along the fuel spray. These flames propagate faster

downstream than they do upstream until the flame stabilizes [28,30]. In contrast, the RANS models features ignition kernels that move upstream, a phenomenon that does not occur in experiments [28,30]. From these conclusions, it appears that both simulations produce acceptable results and the proper model depends on what the user is studying.

## Chapter 3

### 3 Computational Methodology

#### 3.1 Chapter Overview

This chapter focuses on the computational methodology used for this work. It will describe the equations employed by the sensitivity analysis, 0-D simulations and 3-D simulations, in that order. Each section is divided into sub-sections that explain the sub-models used in that analysis.

#### 3.2 Sensitivity Analysis Methodology

In this work, a sensitivity analysis was performed to identify the reactions that significantly impact the ignition delay of the mechanism. Choosing the most critical reactions was important, as changing the reaction rates for these crucial elements should impact the combustion for both 0-D and 3-D models. Thus, Chemkin 17.0 was used to conduct a reaction sensitivity analysis on the ignition delay time for the mechanism. The analysis is best explained in the Chemkin 17.0 Theory manual [32] and will be briefly described herein. An analysis on the reaction rates focuses on the pre-exponential factors ('A-Factors') in the Arrhenius reaction-rate equations. Using the formula to represent the vector of governing equations:

$$F(\Phi(\zeta); \zeta) = 0 \quad (1)$$

where  $F$  is the residual vector,  $\Phi$  is the solution vector, and  $\zeta$  is the model parameter in question (for this study, it is the A-factors). Equation 1 is then differentiated with respect to  $\zeta$  to produce:

$$\frac{\partial F}{\partial \Phi} \frac{\partial \Phi}{\partial \zeta} + \frac{\partial F}{\partial \zeta} = 0 \quad (2)$$

The Jacobian of the of the original matrix is described by  $\frac{\partial F}{\partial \Phi}$ , the sensitivity coefficients are expressed by  $\frac{\partial \Phi}{\partial \zeta}$ , and the partial derivatives of vector  $F$  with respect to the A-factors is given by

$\frac{\partial F}{\partial \zeta}$ . The sensitivity coefficients are resolved in the system of equations shown in Equation 2, and can be normalized based on the greatest value of the dependent variable.

### 3.3 0-D Computation Methodology

This section covers the equations used by the 0-D simulations. These simulations are simple as the volume of the chamber is fixed and no mass flows throughout the chamber. The energy equation is a crucial focus of this investigation as it is expanded to account for the energy released by combustion. The section will review how the governing equations are resolved and discuss how combustion is modeled.

#### 3.3.1 Governing Equations

Chemkin 17.0 was utilized for the 0-D investigation. Again, the Chemkin 17.0 Theory manual [32] is the best source for describing the governing equations but they will be concisely described here. The mechanisms were simulated in a batch reactor model in which the initial gas species were homogeneously mixed inside a constant volume. Mass does not enter or leave this volume for the entirety of the simulation. Therefore, the mass balance in the system can be described by:

$$\frac{d(\rho V)}{dt} = 0 \quad (3)$$

Where  $\rho$  is the density of the mass in the system and  $V$  is the volume of the reactor [32]. Since this investigation is looking into chemical reactions, species are conserved through the following equation:

$$\rho V \frac{dY_k}{dt} = \omega_k V W_k \quad (4)$$



For Equation 4,  $Y_k$  is the mass fraction of the  $k^{\text{th}}$  species,  $\dot{\omega}_k$  is the molar production rate of species  $k$  due to chemical reactions in the gas phase (per unit volume) and  $W_k$  is the molecular weight of species  $k$ . The term  $\dot{\omega}_k$  is defined later in Equation 10. The energy equation, expressed as:

$$\rho V \left[ \bar{c}_p \frac{dT}{dt} \right] = V \sum_{k=1}^K h_k \dot{\omega}_k W_k + V \frac{dP}{dt} \quad (5)$$

is used to express how the temperature and pressure change in the chamber with time.  $\bar{c}_p$  is defined as the mean specific heat term for all gas components and is calculated as:

$$\bar{c}_p = \sum_{k=1}^K Y_k c_{pk} \quad (6)$$

For this investigation, the ignition delay time for the 0-D simulations is defined as the time from the start of the simulation until the time of maximum temperature increase (i.e. when  $\frac{dT}{dt}$  is maximum). The rate of heat released due to the chemical reactions is defined as:

$$\frac{dQ}{dt} = -V * \sum_{k=1}^K h_k \dot{\omega}_k W_k \quad (7)$$

### 3.3.2 Combustion Modeling

The chemical reactions will be explained. As mentioned in [32,33], a basic reaction can be expressed as:



Where  $\nu_k$  is the stoichiometric coefficient of species  $k$  and  $A_k$  is the chemical formula of species  $k$ . The amount of species  $k$  formed during a reaction is expressed as:

$$n_k = n_{k0} + \nu_k \epsilon \quad (9)$$

Where  $n_k$  is the amount of the species at the time in question,  $n_{k0}$  is the initial amount of species  $k$  and  $\epsilon$  is the reaction coordinate which expresses the occurrence of the reaction in question. It is important to note that the sign of convention for the stoichiometric coefficient of the species is different for reactants and products; the reactants have a negative sign convention whereas the products have a positive sign convention. This is to indicate the consumption of the reactants and the production of the products. If there are multiple reactions that consume and produce certain species, the production rate for species  $k$  is expressed by [30]:

$$\dot{\omega}_k = \sum_{r=1}^{\mathcal{R}} V_{k,r} \epsilon_r \quad (10)$$

where  $\mathcal{R}$  is the total amount of reactions that affect species  $k$  and  $V_{m,r}$  is the summation of the stoichiometric coefficients for species  $m$  during reaction  $r$ . To express the progress of the reaction, the reaction coordinate for that reaction is given by:

$$\epsilon_r = q_{forward} \prod_{k=1}^K (X_k)^{\nu_{k,r}} - q_{reverse} \prod_{k=1}^K (X_k)^{\nu'_{k,r}} \quad (11)$$

Where  $X_k$  is the molar concentration of species  $k$  and  $q$  is the forward and reverse rate coefficients for that reaction. In this work, the Arrhenius form of the forward and reverse rate coefficients are used, which is given as:

$$q = AT^b e^{\frac{-E_A}{RT}} \quad (12)$$

Where  $A$  is the pre-exponential factor,  $b$  is the temperature exponent for the given reaction,  $E_A$  is the activation energy and  $R$  is the universal gas constant. This methodology is a highly accurate way of tracking how to combustion develops in the simulation.

### 3.4 3-D Computational Methodology

This section will touch on the methodology used for the turbulent spray combustion simulations. The geometry and mesh used for the simulation will be presented. Following that discussion, the sub-models used for the spray, droplet collision and evaporation, turbulence and combustion will be explained.

#### 3.4.1 Geometry and Mesh Generation

For the 3D analysis, the aforementioned Spray A condition developed by the ECN is used in conjunction with the CFD software CONVERGE [43]. The geometry used for the 3-D simulation was based on Sandia National Lab's constant volume combustion chamber as shown in Figure 3.1. The domain is cylindrical in shape, measuring 80.6 mm in length and diameter.

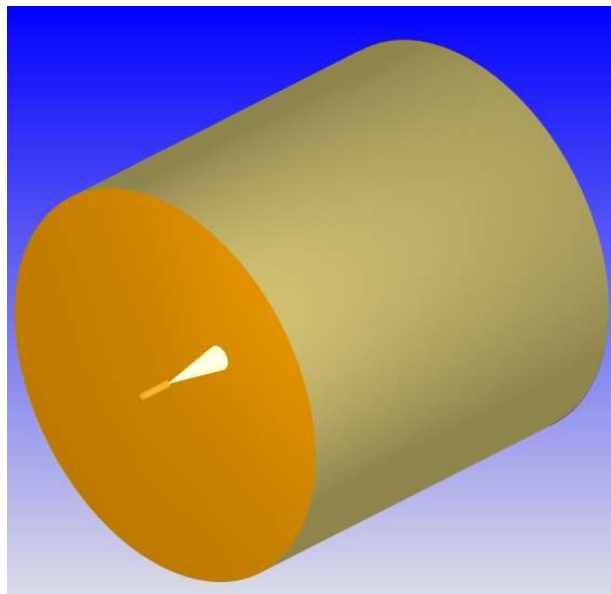


**Figure 3.1 The 3-D computational geometry used for this work.**

The mesh used in the simulations has been evaluated in previous work [37] and will be described herein. A base grid size of 2 mm is used for the domain, and features a heavily embed region around the nozzle. This embed region is 1 mm in diameter and extends 12 mm from the tip

of the nozzle into the chamber. This length was determined based on the steady-state liquid penetration length of the ECN's experimental data [1]. The cells within this region are refined to a size of 31.25  $\mu\text{m}$ . Since it is difficult to predict how the spray will develop outside this embed region, CONVERGE's Adaptive Mesh Refinement (AMR) was utilized to refine cells of interest. This use of additional cells in areas of interest makes AMR a powerful tool. AMR evaluates sub-grid conditions to determine where refinement is needed based on user conditions. The sub-grid is defined by CONVERGE as the difference between the actual field and the resolved field. According to the work of Bedford and Yeo [35] and Pomraning [36] the sub-grid for any scalar can be expressed as an infinite series given as:

$$\begin{aligned} \phi' = & -\alpha_{[k]} \frac{\partial^2 \bar{\phi}}{\partial x_k \partial x_k} + \frac{1}{2!} \alpha_{[k]} \alpha_{[l]} \frac{\partial^4 \phi}{\partial x_k \partial x_k \partial x_l \partial x_l} \\ & - \frac{1}{3!} \alpha_{[k]} \alpha_{[l]} \alpha_{[m]} \frac{\partial^6 \bar{\phi}}{\partial x_k \partial x_k \partial x_l \partial x_l \partial x_m \partial x_m} + \dots \end{aligned} \quad (13)$$

In which,  $\phi'$  is the sub-grid scalar field,  $\alpha_{[k]}$  is  $\frac{dx_k^2}{24}$  for a rectangular cell, the brackets indicate no summation, and  $\bar{\phi}$  is the resolved scalar field. Since it is impossible to evaluate an infinite series, AMR approximates the series using the first term in Equation 13. This results in:

$$\phi' \cong -\alpha_{[k]} \frac{\partial^2 \bar{\phi}}{\partial x_k \partial x_k} \quad (14)$$

For this work, if the sub-grid scale was larger than 2.5 K for temperature and 1 m/s for velocity, AMR refined the cells. AMR was allowed to refine the cells down to a minimum size of 31.25  $\mu\text{m}$ . The total allowable cell count for the simulation was 30 million and was determined through a mesh dependency analysis performed in [37]. In that previous work, it was found that temperature rise caused by combustion would converge if AMR was allowed to refine to 31.25 microns outside the aforementioned embed region and the cell count was allowed to rise to a

minimum of 20 million from a beginning cell count of 0.5 million. This is shown in Figure 3.2. Due to the accuracy required in this work, a maximum allowable cell count of 30 million was allowed. The initial mesh can be seen in Figure 3.3.

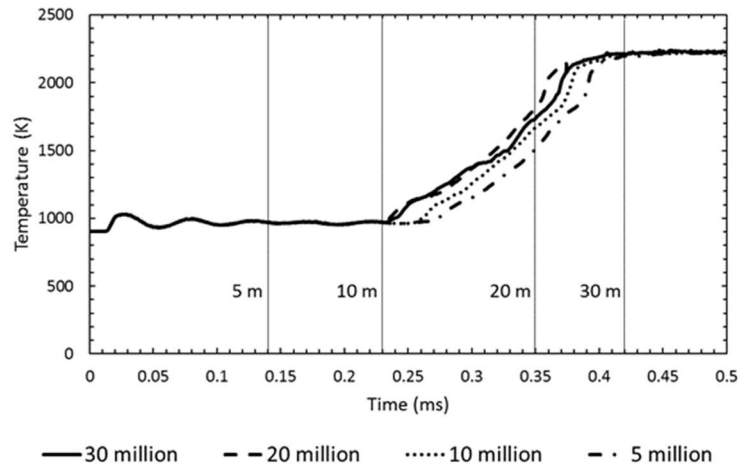


**Figure 3.2 Gas temperature in the combustion chamber using different maximum cell count thresholds. The vertical lines show at which point in the simulation the maximum cell count was achieved [37].**

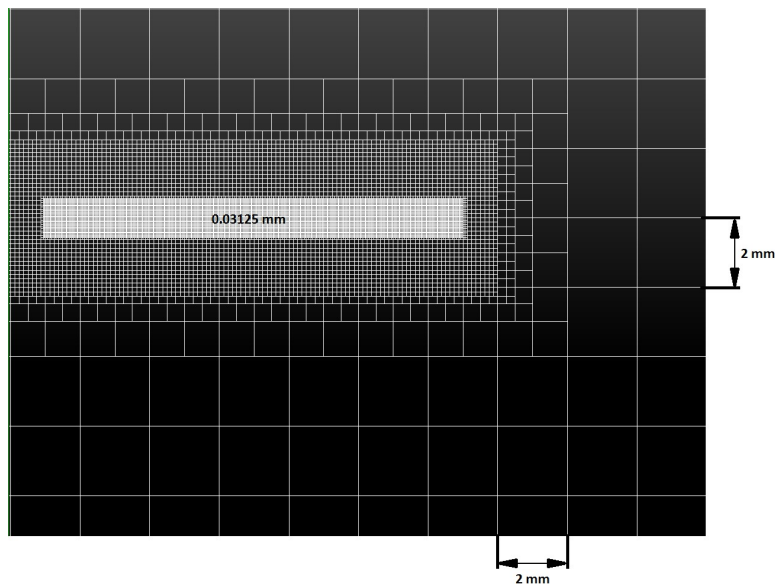


**Figure 3.3 Mesh used for all 3-D cases in the simulation. Mesh size was determined in [37].**

### 3.4.2 Spray Modeling

CONVERGE couples pressure and velocity using the Pressure Implicit with Splitting of Operators (PISO) method developed by Issa [38]. The fuel is injected as a Lagrangian particle into the gas which is represented as a Eulerian field. The liquid and gas are coupled using the nearest computational node of the gas phase to exchange mass, momentum and energy to the parcel. The fuel is injected using the blob injection model of Reitz and Diwakar [39]. This model equates the parcel leaving the injector as the same size of the injector nozzle (i.e. 84  $\mu\text{m}$ ) as seen in Figure 3.4. The break-up of the particle is modeled using the KH-RT model based on the Kelvin-Helmholtz (KH) and Rayleigh-Taylor (RT) instabilities, which will be briefly described herein. The Kelvin-Helmholtz model assumes that the injected parcels are large enough to be modeled as a liquid jet as show in Figure 3.4.

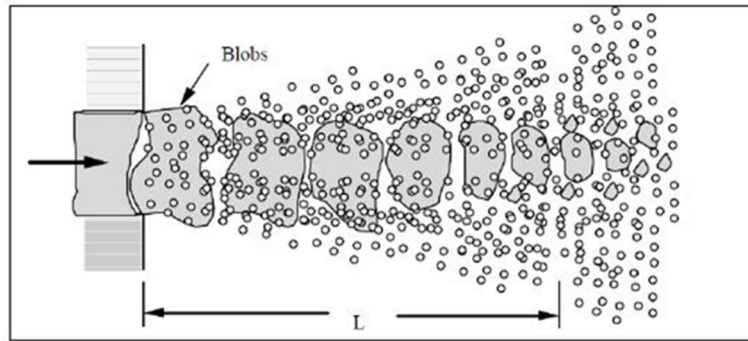


**Figure 3.4 Visualization of blob-injection model of Reitz [40].**

These jets predict unstable waves for certain flow conditions which have maximum growth rate  $\Omega_{\text{KH}}$  and corresponding unstable surface wavelength  $\Lambda_{\text{KH}}$  described by Reitz 1987 [41] as:

$$\frac{\Lambda_{\text{KH}}}{r_p} = 9.02 \frac{(1 + 0.45Z_l^{0.5})(1 + 0.4T^{0.7})}{(1 + 0.87We_g^{1.67})^{0.6}} \quad (15)$$

$$\Omega_{KH} \left[ \frac{\rho_l r_p^3}{\sigma} \right]^{0.5} = \frac{(0.34 + 0.38 We_g^{1.5})}{(1 + Z_l)(1 + 1.4 Ta^{0.6})} \quad (16)$$

where  $Z_l$  is the Ohnesorge number,  $Ta$  is the Taylor number,  $We$  is the Weber number,  $\sigma$  is the surface tension, and  $r_p$  is the radius of the parcel. Subscripts  $l$  and  $g$  represent the liquid and gas phase respectively. These instabilities will impact how quickly the injected parcels changes size. As aforementioned, the parcels are equal to that of the nozzle diameter but will breakup to a radius ( $r_d$ ) proportional to the wavelength of the unstable surface described by:

$$r_d = B_0 \Lambda_{KH} \quad (17)$$

$B_0$  is a model constant that was set to 0.6 for this work and was based on the work of Reitz 1987 [41]. The rate of change of the parent parcel radius is described as:

$$\frac{dr_p}{dt} = -\frac{(r_p - r_d)}{\tau_{KH}}, \quad (r_d \leq r_p) \quad (18)$$

where the breakup time is defined as:

$$\tau_{KH} = \frac{3.762 B_1 r_p}{\Lambda_{KH} \Omega_{KH}} \quad (19)$$

$B_1$  is a model constant that defines the initial fuel jet disturbance level that varies between fuel injectors [42]. For this investigation, this constant was set as 4. As the jet of fuel inserts into the chamber, the RT instabilities occur after a defined break-up length of the liquid core. This length is defined as:

$$L_b = C_b \sqrt{\frac{\rho_l}{\rho_g}} d_0 \quad (20)$$

where the constant  $C_b$  is equal to 10 for this study and  $d_0$  is the diameter of the nozzle. This breakup length is depicted in Figure 3.5.

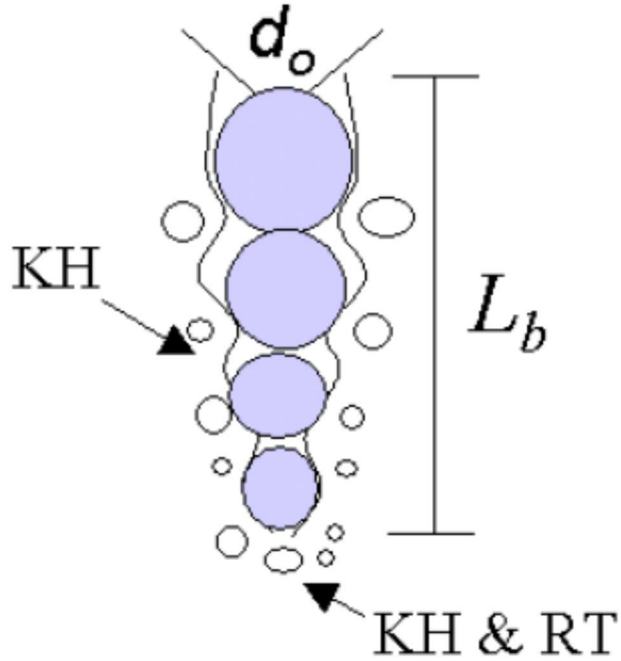


**Figure 3.5** Depiction of the KH-RT breakup length model. Prior to length  $L_b$ , the Kelvin-Helmholtz instabilities only impact the breakup of the spray. After this length, the Rayleigh-Taylor instabilities also impact the spray breakup [43].

After this defined length, both KH and RT instabilities occur. The Rayleigh-Taylor are assumed to be caused by the magnitude of the drag for on the droplet. Similar to the KH model, the RT instabilities are modeled as waves occurring on the droplet surface. CONVERGE uses the study of Xin et al. 1998 [44] to define the fastest growing wavelength and corresponding growth rate of these instabilities as:

$$\Lambda_{RT} = 2\pi \sqrt{\frac{3\sigma}{a(\rho_l - \rho_g)}} \quad (21)$$

and

$$\Omega_{RT} = \sqrt{\frac{2[a(\rho_l - \rho_g)]^{-3/2}}{3\sqrt{3}\sigma(\rho_l + \rho_g)}} \quad (22)$$



respectively. For Equations 21 and 22,  $a$  is defined as the droplet deceleration. If the wavelength defined by  $C_{RT}\lambda_{RT}$  is calculated to be smaller than diameter of the droplet, the model assumes that the RT waves are growing on the surface of the droplet. If these waves are allowed to remain on the droplet surface for a time equal to  $\frac{C_t}{\Omega_{RT}}$ , the RT instabilities are assumed to break-up the droplet. For this study, the constants  $C_{RT}$  and  $C_t$  are 0.1 and 1.0, respectively.

### 3.4.3 Droplet Collision Modeling

In addition to the droplets of the spray breaking up, they are also subjected to collisions. The collisions are modeled based on the No Time Counter (NTC) model of Schmidt and Rutland 2000 [45], as will be briefly described. Derived from probability model for stochastic collision, the NTC model sorts the number of parcels that reside within a computational cell. The expected number of collisions within a cell is deduced by summing the probability of all possible collisions. For a cell with  $N$  droplets which have cross-section of  $\sigma_{i,j} = \pi(r_i + r_j)^2$  during a time interval of  $\Delta t$  this is expressed as:

$$M_{collision} = \frac{1}{2} \sum_{i=1}^N \sum_{j=1}^N \frac{v_{i,j} \sigma_{i,j} \Delta t}{\mathcal{V}} \quad (23)$$

where  $v_{i,j}$  is the relative velocity between the two droplets and  $\mathcal{V}$  is the cell volume. By grouping similar droplets together in a parcel, assuming that all the droplets within a parcel have uniform physical properties and simplifying the equation to allow for a constant factor to be outside of the summations, the equation is now represented as:

$$M_{collision} = \frac{(wv\sigma)_{max}\Delta t}{2\mathcal{V}} \sum_{i=1}^{N_p} w_i \sum_{j=1}^{N_p} \frac{w_j v_{i,j} \sigma_{i,j}}{(qV\sigma)_{max}} \quad (24)$$

where  $N_p$  is the number of parcels within the cell and  $w$  is the number of droplets within a parcel.  $(wv\sigma)_{max}$  scales the selection probability of a collision and must be large enough so that the following is true:

$$\frac{w_j v_{i,j} \sigma_{i,j}}{(wv\sigma)_{max}} < 1 \quad (25)$$

If this is true, it can be assumed that a representative sub-sample of parcels within the computational cell can represent all parcels within the cell. This reduces the limits of summation, and the amount of collisions within the cell can be expressed as:

$$M_{collision} = \sum_{i=1}^{\sqrt{M_{assump}}} w_i \sum_{j=1}^{\sqrt{M_{assump}}} \frac{w_j v_{i,j} \sigma_{i,j}}{(wv\sigma)_{max}} \quad (26)$$

where:

$$M_{assump} = \frac{N_p^2 (wv\sigma)_{max} \Delta t}{2\psi} \quad (27)$$

Equation 24 is used by CONVERGE to calculate the collisions of the droplets within this investigation. To determine what happens to the droplets after a collision occurs, the model of Post and Abraham 2002 [46] is utilized and will be described succinctly. This model predicts the following outcomes for the droplets: grazing collision, coalescence, stretching separation and reflexive separation. To determine what occurs after the collision, the collision Weber number ( $We_{collision}$ ) is compared to a bouncing Weber number described by:

$$We_{bounce} = \frac{\Delta_p (1 + \Delta_p^2) (4\phi - 12)}{\chi_1 (\cos(\arcsin B))^2} \quad (28)$$

where:

$$\Delta_p = \frac{r_1}{r_2} \quad (r_2 > r_1) \quad (29)$$

$$\varphi = \varphi_0 \left( \frac{\rho_g}{\rho_0} \right)^{\frac{2}{3}} \quad (30)$$

$$\chi_1 = 1 - 0.25(2 - \tau)^2(1 + \tau) \quad \text{for } \tau > 1 \quad (31)$$

$$\chi_1 = 0.25\tau^2(3 - \tau) \quad \text{for } \tau < 1$$

and:

$$\tau = \frac{1 - B}{1 + \Delta_p} \quad (32)$$

For equation 30,  $\varphi_0$  is 3.351,  $\rho_0$  is  $1.16 \frac{kg}{m^3}$ , and  $\rho_g$  is the gas density.  $B$  is given by:

$$B = \frac{b}{r_1 + r_2} \quad (33)$$

where  $b$  is the distance from the center of one drop to the relative velocity vector placed on the center of the other drop.  $r_1$  and  $r_2$  are the droplet radii for the colliding droplets. Figure 3.6 provides a visual of  $b$  as provided by Post and Abraham [46].

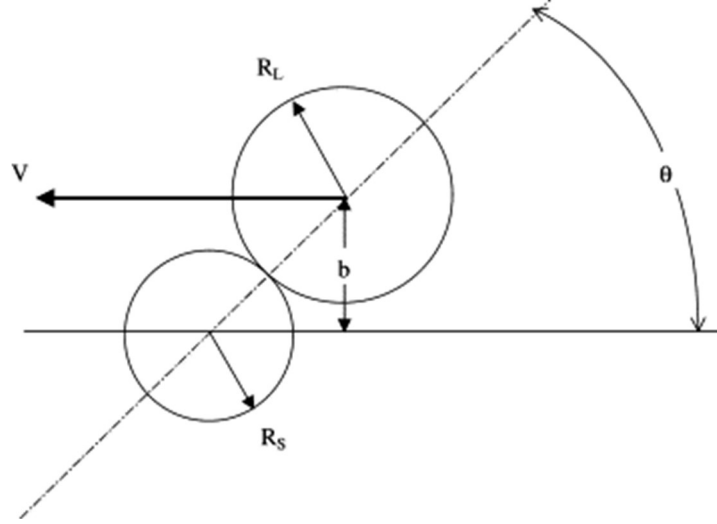


**Figure 3.6** Figure of droplet-droplet collision. This depiction shows how CONVERGE calculates the post-collision direction and velocity of the droplets as outlined in the above equations. Image adopted from [46] with permission.

Once  $We_{bounce}$  has been determined, the droplets are assumed to bounce if  $2We_{collision} < We_{bounce}$  [47], or either coalesce, separate by stretching or separate by reflex if  $2We_{collision} \geq We_{bounce}$ . To determine which of the latter events occur, CONVERGE checks two other criteria. Stretching separation occurs if  $b > b_{critical}$ , while reflexive separation can occur if the criterion of Ashgriz and Poo (1990) [48] is met. This criterion is defined as:

$$2We_{collision} > 3 \left[ 7(1 + \Delta_p^3)^{\frac{2}{3}} - 4(1 + \Delta_p^2) \right] \frac{\Delta_p (1 + \Delta_p^3)^2}{\Delta_p^6 \eta_1 + \eta_2} \quad (34)$$

where:

$$\eta_1 = 2(1 - \xi)^2 \sqrt{1 - \xi^2} - 1 \quad (35)$$

$$\eta_2 = 2(\Delta_p - \xi)^2 \sqrt{\Delta_p^2 - \xi^2} - \Delta_p^3 \quad (36)$$

and

$$\xi = 0.5B(1 + \Delta_p) \quad (37)$$

For all cases, the post-collision velocities are expressed as:

$$v_{i,1}' = \frac{m_1 v_{i,1} + m_2 v_{i,2} + m_2 (v_{i,1} - v_{i,2})}{m_1 + m_2} \sqrt{1 - f_E} \quad (38)$$

and,

$$v_{i,2}' = \frac{m_1 v_{i,1} + m_2 v_{i,2} + m_1 (v_{i,2} - v_{i,1})}{m_1 + m_2} \sqrt{1 - f_E} \quad (39)$$

As described in the work of Hou [47]. For these equations,  $f_e$  is the amount of energy lost in the collision represented as a fraction. In the cases where the droplets bounce,  $f_E = 0$ . However, if CONVERGE determines that only stretching separation occurs,  $f_E$  can be found through:

$$1 - f_E = \left( \frac{b - b_{critical}}{1 - b_{critical}} \right)^2 \quad (40)$$

Similarly, if reflexive separation is the only determined outcome of the collision, then  $f_E$  can be found through:

$$1 - f_E = 1 - \frac{3 \left[ 7(1 + \Delta_p^3)^{\frac{2}{3}} - 4(1 + \Delta_p^2) \right] \frac{\Delta_p (1 + \Delta_p^3)^2}{\Delta_p^6 \eta_1 + \eta_2}}{2We_{collision}} \quad (41)$$

Both equations of  $f_E$  are determined in the work of Hou [47]. If CONVERGE finds that  $2We_{collision} \geq We_{bounce}$  but neither form of separation occurs, the droplets are assumed to coalesce.

The droplet-wall interaction is modeled by wall impingement model of Gonzalez et al. 1991 [49]. However, the walls of the computational domain are sufficiently far away that wall-droplet interaction does not occur. Thus, discussion of this model has been omitted.

### 3.4.4 Droplet Evaporation Modeling

As the liquid droplets are dispersed throughout the domain, they will eventually evaporate. In this study, the Frossling correlation is used to determine the how the mass of the fuel evaporates into the domain based on the study of Amsden et al. [50]. From this study, the rate of change of the droplet radius is defined as:

$$\frac{dr_0}{dt} = -\frac{\rho_g D}{2\rho_l r_0} B_d Sh_d \quad (42)$$

where  $D$  is the mass diffusivity of the liquid vapor in air,  $B_d$  is the ratio of vapor mass fractions and  $Sh_d$  is the Sherwood number.  $B_d$  is expressed as:

$$B_d = \frac{Y' - Y}{1 - Y} \quad (43)$$

where  $Y'$  is the vapor mass fraction at the droplet surface and  $Y$  is the vapor mass fraction of the ambient gas. Furthermore  $Sh_d$  is defined as:

$$Sh_d = (2 + 0.6Re_d^{\frac{1}{2}}Sc^{\frac{1}{3}}) \frac{\ln(1 + B_d)}{B_d} \quad (44)$$

in which:

$$Re_d = \frac{\rho_g |u_i + u_i - v_i'| 2r_d}{\mu_{air}} \quad (45)$$

and  $Sc$  is the Schmidt number of air. The air viscosity term in the Reynold's number formulation and the Schmidt number are evaluated at a temperature calculated by:

$$T_\mu = \frac{T_g + 2T_d}{3} \quad (46)$$

where  $T_g$  is the temperature of the ambient gas and  $T_d$  is the temperature of the droplet. The mass diffusivity term in Equation 40 and the Schmidt number can be found from:

$$\rho_g D = 1.293 D_0 \left( \frac{T_\mu}{273} \right)^{n_0 - 1} \quad (47)$$

$D_0$  and  $n_0$  are experimentally determined model constants, which are  $4.16 \cdot 10^{-6}$  and 1.6 respectively for this study. In CONVERGE,  $Y'$  in Equation 43 is defined by:

$$Y' = \frac{M_{fuel}}{W_{fuel} + W_{mix} \left( \frac{P_g}{P_v} - 1 \right)} \quad (48)$$

where  $W_{fuel}$  is the molar weight of the fuel,  $W_{mix}$  is the molar weight of the mixture,  $P_g$  is the pressure of the gas, and  $P_v$  is the vapor pressure at the current droplet temperature. Overall, these equations model the mass shedding of the droplet over time as the droplet evaporates.

### 3.4.5 Turbulence Modeling

For this work, the Re-Normalisation Group (RNG) k- $\epsilon$  RANS turbulence model was used for CONVERGE [43]. As it is well known, RANS models express instantaneous qualities of the flow as fluctuations around an ensemble average term determined by averaging Navier-Stokes equations. The mass and momentum transport equations used by CONVERGE are:

$$\frac{\partial \bar{\rho}}{\partial t} + \frac{\partial \bar{\rho} \tilde{u}_j}{\partial x_j} = 0 \quad (49)$$

and,

$$\frac{\partial \bar{\rho} \tilde{u}_i}{\partial t} + \frac{\partial \bar{\rho} \tilde{u}_i \tilde{u}_j}{\partial x_j} = - \frac{\partial \bar{P}}{\partial x_i} + \frac{\partial}{\partial x_j} \left[ \mu \left( \frac{\partial \tilde{u}_i}{\partial x_j} + \frac{\partial \tilde{u}_j}{\partial x_i} \right) - \frac{2}{3} \mu \frac{\partial \tilde{u}_k}{\partial x_k} \delta_{ij} \right] + \frac{\partial}{\partial x_j} \tau_{ij} \quad (50)$$

respectively. The Reynolds stress term for the RNG RANS model is given as:

$$\tau_{ij} = 2\mu_t S_{ij} - \frac{2}{3}\delta_{ij} \left( \rho k + \mu_t \frac{\partial \tilde{u}_i}{\partial x_i} \right) \quad (51)$$

where  $S_{ij}$  is the mean strain rate tensor, and  $\mu_t$  is the turbulent viscosity. These terms are defined as:

$$S_{ij} = \frac{1}{2} \left( \frac{\partial \tilde{u}_i}{\partial x_j} + \frac{\partial \tilde{u}_j}{\partial x_i} \right) \quad (52)$$

and

$$\mu_t = c_\mu \rho \frac{k^2}{\varepsilon} \quad (53)$$

where  $c_\mu$  is a model constant which was 0.0845 for this study. The turbulent kinetic energy and dissipation of turbulent kinetic energy transport equations are expressed as:

$$\frac{\partial \rho k}{\partial t} + \frac{\partial \rho u_i k}{\partial x_i} = \tau_{ij} \frac{\partial u_i}{\partial x_j} + \frac{\partial}{\partial x_j} \frac{\mu}{Pr_k} \frac{\partial k}{\partial x_j} - \rho \varepsilon + \frac{c_s}{1.5} S_s \quad (54)$$

and

$$\begin{aligned} \frac{\partial \rho \varepsilon}{\partial t} + \frac{\partial \rho u_i \varepsilon}{\partial x_i} &= \frac{\partial}{\partial x_j} \left( \frac{\mu}{Pr_\varepsilon} \frac{\partial \varepsilon}{\partial x_j} \right) + c_{\varepsilon 3} \rho \varepsilon \frac{\partial u_i}{\partial x_i} \\ &+ \left( c_{\varepsilon 1} \frac{\partial u_i}{\partial x_j} \tau_{ij} - c_{\varepsilon 2} \rho \varepsilon + c_s S_s \right) \frac{\varepsilon}{k} + S - \rho R \end{aligned} \quad (55)$$

In the aforementioned equations,  $c_{\varepsilon 1}$ ,  $c_{\varepsilon 2}$ , and  $c_{\varepsilon 3}$  are model constants that are used to account for compression and expansion. They are 1.42, 1.68, and -1.0 for this work.  $S$  and  $S_s$  are user-supplied source terms that interact with the spray. For this work,  $S$  set as 0 and  $S_s$  is 0.03.  $R$  is defined as:

$$R = \frac{c_\mu \eta^3 \left( 1 - \frac{\eta}{\eta_0} \right) \varepsilon^2}{(1 + \beta \eta^3) k} \quad (56)$$



where:

$$\eta = \frac{k}{\varepsilon} \sqrt{2S_{ij}S_{ij}} \quad (57)$$

Note that  $\beta$  and  $\eta_0$  are model constants, which are 0.012 and 4.38 respectively for this work.

Equations 56 and 57 are unique to the RNG RANS model [43].

### 3.4.6 Combustion Modeling

CONVERGE features a detailed chemistry solver named SAGE. SAGE models chemical kinetics based on reaction thermodynamic data that is in the CHEMKIN format. To calculate the combustion, SAGE calculates the reactions rates for each elementary reaction and solves the combustion using the CVODES solver, while the other parts of the CFD package calculate the transport equations of these species. It should be noted that for this work, the turbulence chemistry interaction has been ignored, regardless of its significance. The methodology of SAGE is 0-D, which has been explained in the previous section and therefore will not be explained herein.

## Chapter 4

### 4 Results and Discussion

#### 4.1 Chapter Overview

This chapter discusses the results of the simulations. It will lead with the results validating the kinetic mechanisms used in this investigation. Following this investigation, the results of the sensitivity analysis are presented as well as the results of the 0-D and 3-D simulations. The chapter is divided into two sub-sections based on the results of the sensitivity analysis and the results of the combustion simulations.

#### 4.2 Sensitivity Analysis

In this study, the n-dodecane kinetic mechanisms of Narayanaswamy et al. [51] was utilized. To reduce computational time, the mechanism was reduced from 369 species and 1896 reactions to 109 species and 169 reactions. This newly developed reduced mechanism and the mechanism of Narayanaswamy et al. [51] were validated against experimental shock tube data from the Oehlschlager group as reported in [52]. The mechanisms simulated a 0-D constant volume chamber as discussed in the previous chapter at temperatures from 800 to 1100 K at 100° intervals. The pressures for these temperatures were 40, 60, and 80 atm, and the equivalence ratio varied between 1 and 2. These conditions were the same as the experiments [52]. As seen in Figures 4.1 and 4.2, both mechanisms' ignition delays were in fair agreement with the experimental data for most test conditions. The exception would be the test conditions in the low temperature regions, where both mechanisms struggled to predict the experimental data.

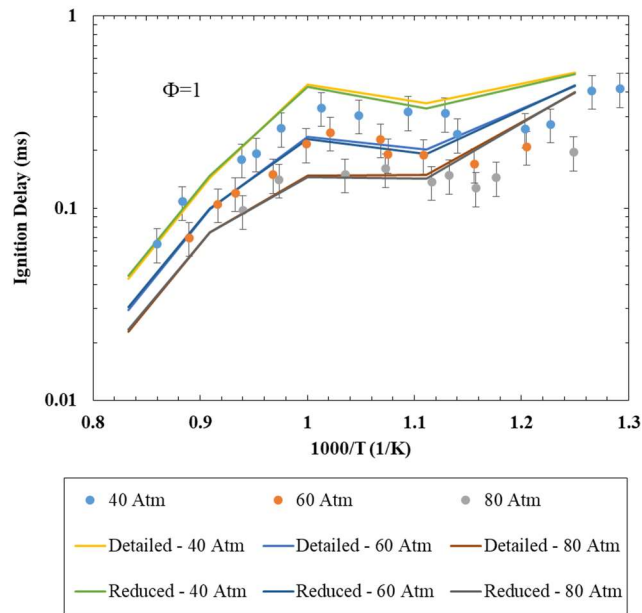


**Figure 4.1 Simulations and experimental ignition delay at an equivalence ratio of 1. N-dodecane is the fuel used in this study.**

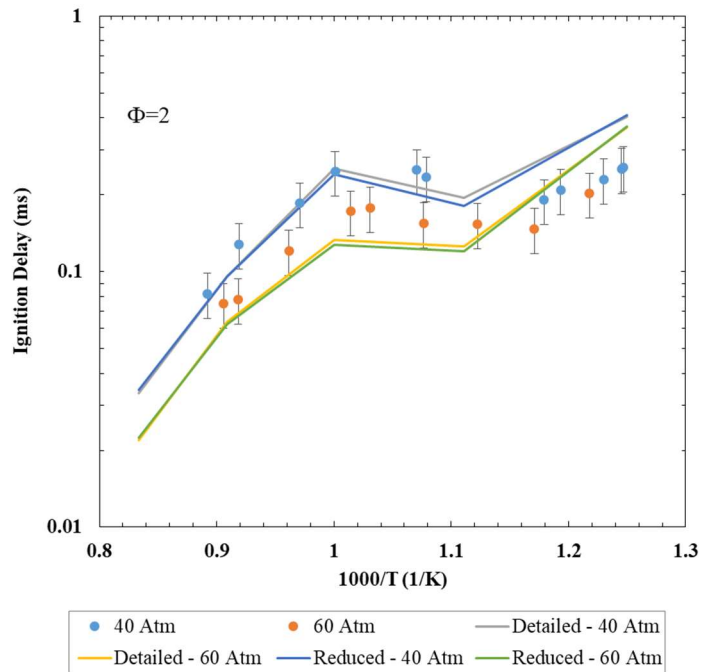


**Figure 4.2 Simulations and experimental ignition delay at an equivalence ratio of 2. N-dodecane is the fuel used in this study.**

Since the newly developed skeletal mechanism succeeded in predicting the ignition delay of the experimental data for a wide range of conditions to the same degree of accuracy as the parent mechanism of Narayanaswamy et al., it was deemed suitable for further analysis in this investigation.

The skeletal mechanism was subjected to a sensitivity analysis at temperatures of 800 to 1400 K and pressures of 10 to 60 bar. The sensitivity analysis would individually alter each reaction in the mechanism to the same degree, and compare the new ignition delay to that of the mechanism before the reaction rate was modified. For this investigation, a modified reaction which produced a change to the ignition delay of greater than  $\pm 10\%$  when compared to the unmodified ignition delay was deemed a critical reaction in the mechanism. Using this criteria, over 30 reactions were identified as critical. Due to the amount of further testing required for this work, the six reaction pathways that produced the greatest change in the ignition delay were used. These reactions can be found in Table 1. Most the reactions decreased the ignition delay (denoted by the negative percent change) with the exception of one reaction ( $C_{12}H_{25}O_2 \rightarrow C_{12}OOH-T6$ ) which increased the ignition delay.

**Table 4.1 Critical Reactions.**

<b>Name</b>	<b>Reaction</b>	<b>Original Reaction Rate</b>
Mechanism 0	$C_{12}H_{25}O_2 \rightarrow C_{12}OOH-T6$	6.904e11
Mechanism 1	$C_{12}H_{25}O_2 \rightarrow C_{12}H_{24} + HO_2$	1.905e38
Mechanism 2	$C_{12}OOHO_2 \rightarrow C_{12}KET-T6 + OH$	3.667e11
Mechanism 3	$NC_{12}H_{26} + HO_2 \rightarrow C_{12}H_{25} + H_2O_2$	3.518e02
Mechanism 4	$CH_3 + HO_2 \leftrightarrow CH_3O + OH$	1.000e13
Mechanism 5	$H + O_2 \leftrightarrow O + OH$	1.040e14

To ensure the effect of the identified reactions on the combustion was observable, the A-factor of each reaction was multiplied by 10 independently of each other in six new mechanism

files. This would amplify the effect of the reaction on the combustion and make the results easier to compare to the original skeletal mechanism.

### 4.3 0-D and 3-D Combustion Simulations

After the sensitivity analysis was performed, the combustion simulations of the new mechanisms were performed in 0-D and 3-D environments. All mechanisms were tested at similar conditions for both cases. The tested ambient temperatures ranged from 900 to 1100 K at 100° intervals, while the pressure remained constant at 60 bar for all tested cases. The ambient gases consisted of the following mass fractions: O<sub>2</sub> = 16.418%, N<sub>2</sub> = 71.975%, CO<sub>2</sub> = 9.376% and H<sub>2</sub>O = 2.331%. A summary of the initial conditions for both cases can be seen in Table 4.2.

**Table 4.2 A summary of initial conditions used for the simulations.**

	0-D Simulation	3-D Simulation
Ambient Composition (% Mass)	16.418% O <sub>2</sub> , 71.975% N <sub>2</sub> , 0.9376% CO <sub>2</sub> , 0.2231% H <sub>2</sub> O	
Ambient Temperature (K)	900 – 1100	
Ambient Pressure (Bar)	60	
Fuel	n-Dodecane (109 species & 169 reactions)	
Equivalence Ratio	1	N/A
Injection Parameters	N/A	Injection Pressure: 1500 Bar Injection duration/mass: 1.5 ms / 3.5 mg
Nozzle Diameter	N/A	90 μm

The ignition delay for the 0-D cases was calculated based on the point of maximum pressure rise with respect to time (i.e. maximum  $\frac{dP}{dt}$ ) in the combustion chamber. The ignition delay for the turbulent spray combustion cases was calculated by the concentration history of the hydroperoxyalkyl radicals, as discussed by Samimi-Abianeh et al. [23] and described herein. Since the fuel is at a much lower temperature than the ambient gas, the vaporized fuel initially undergoes low temperature combustion. During this time, the hydrocarbon fuel undergoes hydrogen abstraction to form alkyl radicals. These radicals obtain oxygen from the ambient gas forming  $RO_2$ , which undergoes isomerization to form a hydroperoxyalkyl. During low temperature combustion, these alkyls multiply and form a peak concentration. However, as the temperature begins to increase, the  $RO_2$  radicals begin to decompose and form  $HO_2$  and  $H_2O_2$  species.  $H_2O_2$  further decomposes as the temperature increases and forms two OH radicals, indicating that high temperature combustion has begun. During this process, the hydroperoxyalkyl radicals reach a post-peak minimum concentration value that aligns nicely with luminosity-based ignition delay. This process can be seen in Figure 4.3. [23] has shown that this method for calculating ignition delay is more representative of experimental data; resultantly, this methodology will be used for calculating the turbulent spray ignition delay in this work.

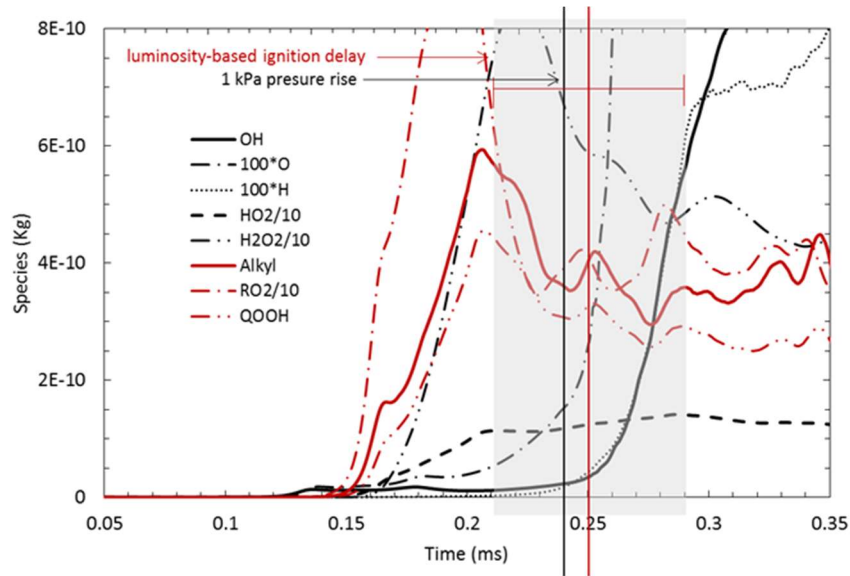


**Figure 4.3 Mass history of key species in the combustion chamber. Initial ambient gas temperature was 1000 K. The ignition delay predicted by the species history is shown in red. As a comparison, the pressure-based ignition delay is shown as well. The luminosity-based ignition delay timing and its respective uncertainty is shown by the gray box. This figure is adopted from [23] with permission.**

The ignition delay times for all modified mechanisms can be seen in Table 4.3. Note that a negative sign denotes a decrease in the new ignition delay when compared to the base mechanism. From the data presented, there exists a disparity between the 0-D predicted ignition delay and the 3-D predicted ignition delay for all tested conditions. The following observations are determined from the table:

$C_{12}H_{25}O_2 \rightarrow C_{12}OOH-T6$ : Modifying the Arrhenius constant by an order of magnitude decreases the ignition delay for the 0-D and 3-D models by an order of magnitude. It should be noted that the 3-D ignition delay is less impacted by the change at temperatures of 900 K and 1000 K. At 1100 K, the opposite is true suggesting that the reaction is dependent on ambient temperature for the spray model.

$C_{12}H_{25}O_2 \rightarrow C_{12}H_{24} + HO_2$ : Increasing the A-factor of the reaction by an order of magnitude increases the ignition delay of both models. However, the 0-D model will have an increase of one order of magnitude but the 3-D model will have an ignition delay change of two orders of magnitude.

$C_{12}OOHO_2 \rightarrow C_{12}KET-T6 + OH$ : Similar to the first reaction mentioned, an order of magnitude change to the rate constant induces an order of magnitude decrease for the ignition delay of both 0-D and 3-D models. The 3-D model is more impacted at higher temperatures, whereas the 0-D model is more impacted at lower temperatures.

$N-C_{12}H_{26} + HO_2 \rightarrow C_{12}H_{25} + H_2O_2$ : When the Arrhenius constant is modified by an order of magnitude, the 0-D and 3-D ignition delays decrease. The 0-D model predicts that ignition delay reaches its lowest value at a temperature of 1000 K, while the 3-D model predicts that the ignition delay continuously decreases as the temperature of the chamber decreases.

$CH_3 + HO_2 \leftrightarrow CH_3O + OH$ : Modifying this rate constant does not impact the ignition delay of the spray for ambient temperatures of 900 K and 1000 K. However, a significant decrease in the ignition delay is observed for the 3-D model at 1100 K. Juxtaposed, the 0-D model appears to have a parabolic change in the ignition delay for the temperature range tested on this ignition delay.

$H + O_2 \leftrightarrow O + OH$ : This reaction impacts both 0-D and 3-D reactions to a similar degree at higher temperature (1100 K). However, the 0-D model shows a decrease in the ignition delay at the lower temperatures whereas the 3-D model shows no significant change in the ignition delay time.



**Table 4.3 Ignition delays of mechanisms with modified reaction rates. Note how the 0-D predictions do not line up with the 3-D predictions.**

	$C_{12}H_{25}O_2 \rightarrow C_{12}OOH$ -T6		$C_{12}H_{25}O_2 \rightarrow C_{12}H_{24} + HO_2$		$C_{12}OOHO_2 \rightarrow C_{12}KET-T6 + OH$		$nC_{12}H_{26} + HO_2 \rightarrow C_{12}H_{25} + H_2O_2$		$CH_3 + HO_2 \leftrightarrow CH_3O + OH$		$H + O_2 \leftrightarrow O + OH$	
Temperature (K)	0-D (%)	3-D (%)	0-D (%)	3-D (%)	0-D (%)	3-D (%)	0-D (%)	3-D (%)	0-D (%)	3-D (%)	0-D (%)	3-D (%)
900	-72	-44	638	>133	-55	-26	-41	-11	-13	1	-13	4
1000	-77	-54	74	>80	-59	-36	-66	-25	-7	0	-12	0
1100	-29	-62	4.1	>110	-17	-40	-55	-37	-14	-24	-23	-25

Figure 4.4 and 4.5 shows the impact these reactions have on the ignition delay when compared to the baseline mechanism. At a time of 0.285 ms after the start of injection (ASOI), at an ambient gas temperature of 1000 K, all mechanisms show their individual combustion progress. As demonstrated in the figure, most of the tested mechanisms accelerated the combustion when compared to the baseline mechanism. This is most evident in the  $C_{12}H_{25}O_2 \rightarrow C_{12}OOH$ -T6,  $C_{12}OOHO_2 \rightarrow C_{12}KET$ -T6 + OH, and  $n$ - $C_{12}H_{26} + HO_2 \rightarrow C_{12}H_{25} + H_2O_2$  reactions, where the combustion is completely underway at the time the images were visualized. As described above and shown in Figure 7, the  $C_{12}H_{25}O_2 \rightarrow C_{12}H_{24} + HO_2$  reaction significantly delays the combustion, as the fuel still propagates within the chamber without reacting compared to the baseline mechanism which is reacting. There is some increased reactivity in the  $CH_3 + HO_2 \leftrightarrow CH_3O + OH$  and  $H + O_2 \leftrightarrow O + OH$  reactions at this ambient temperature. However, they are closely related to the baseline mechanism as described in Table 4.3.

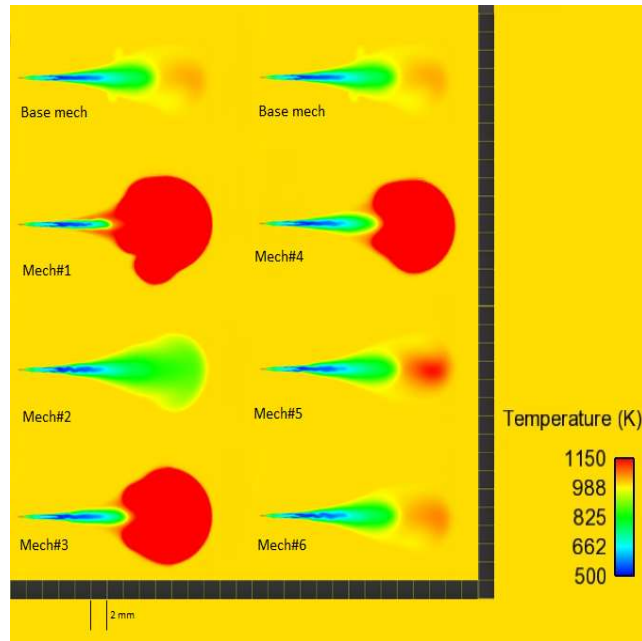


**Figure 4.4 Comparison of the temperature contours of the different mechanisms compared to the baseline mechanism. These contours were visualized 0.285 ms after the start of injection at an initial gas temperature of 1000 K.**

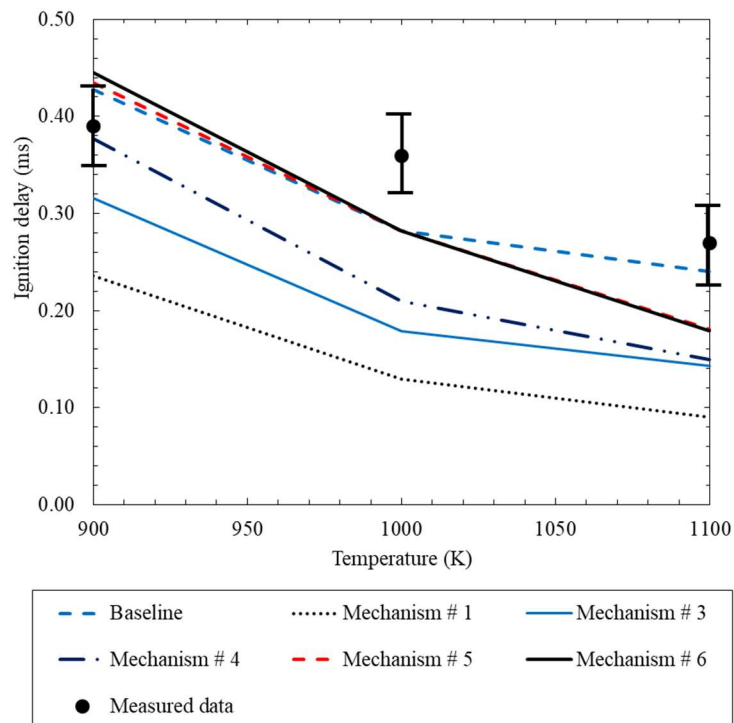


**Figure 4.5 Ignition delays of the turbulent spray simulations using the different mechanisms compared to experimental data [1].**

Since these reactions modified the ignition delay of the spray combustion, it would be a failure of inquiry to ask how the other spray characteristics were impacted by the change in the reaction rates. Following the ignition delay observations, the liquid and vapor penetration lengths were examined for each of the modified mechanisms and compared to experimental data. These lengths for the simulations at 900 K are shown in Figure 9. For this study, the liquid penetration length is defined as the distance from the nozzle that 99% of the n-dodecane mass is contained in. The vapor penetration length is defined as the further distance from the nozzle in which 0.1% of the fuel by mass can be found. As seen in Figure 4.6, the liquid penetration lengths for all mechanisms are very close to one another. This is expected as the liquid penetration length is not impacted by the chemical mechanism. However, the fuel vapor penetration lengths are different for all cases. If the reactivity of the mechanism was found to increase (i.e. the ignition delay was reduced) the fuel vapor penetration length of that mechanism was reduced significantly. This is attributed to the increased rate of radical production that results in an increased consumption rate of the fuel. Reactions that have this increased reactivity (i.e. most of the reactions) show reduced fuel vapor penetration rate when compared to the baseline mechanism. On the other hand, since the  $C_{12}H_{25}O_2 \rightarrow C_{12}H_{24} + HO_2$  reaction impedes the combustion, the vapor continues to disperse into the chamber, resulting in an ever-expanding vapor penetration length.

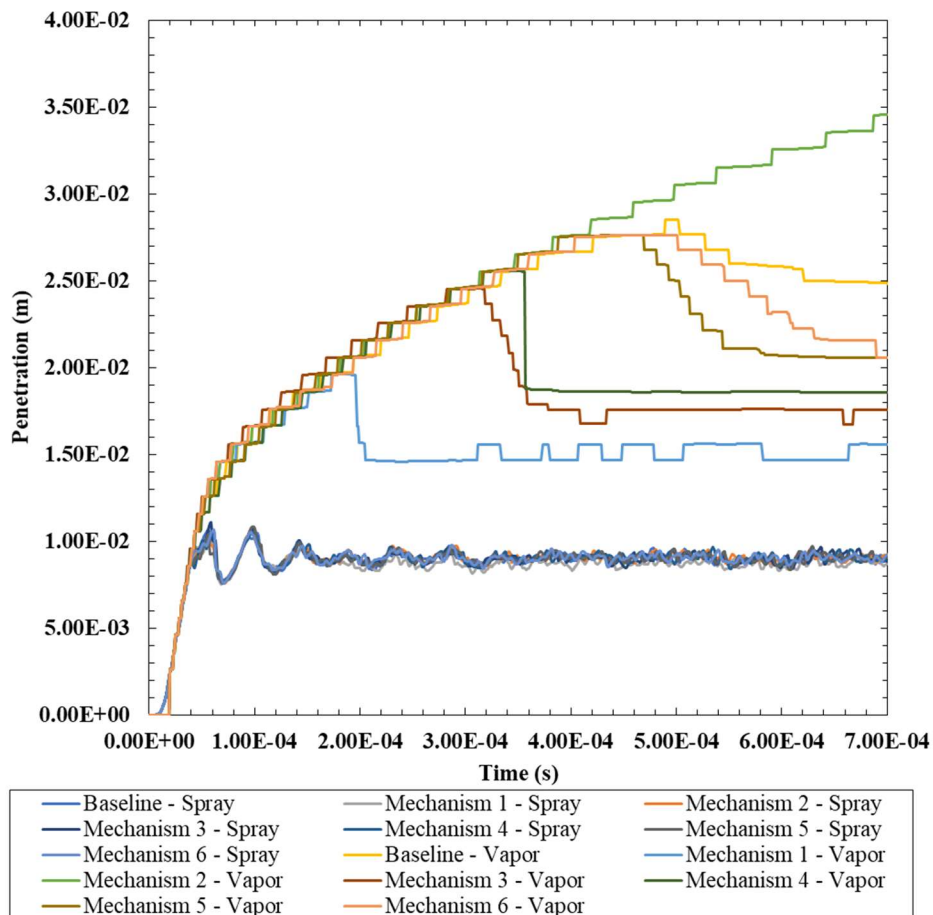


**Figure 4.6 Liquid and vapor penetration lengths of the various mechanisms at an ambient temperature of 900 K.**

A final comparison of flame LOL was conducted to completely scrutinize the data presented by the simulations. In this work, the definition of flame lift-off length was taken from Samimi-Abianeh et al. [23] and will be briefly described here. As explained in the ignition delay section, when the hydroperoxyalkyl radicals are formed the temperature within the chamber increases due to the energy released during this process. The temperature plateaus around a local maximum until high-temperature chemistry begins and the temperature dramatically rises. Furthermore, since the spray is injected into the chamber the chemical reactions can be thought of as occurring at approximately the same axial distance from the nozzle as the heat transfer from the

ambient gas to the fuel should occur at the same rate for similarly sized droplets. It is reasonable, in turn, to assume that the time it takes for the temperature of the fuel vapor to reach this local maximum is the same. This observation was confirmed in the work of Samimi-Abianeh et al. [23], who determined the temperature thresholds for initial ambient gas temperatures of 900, 1000, 1100, and 1200 K are 1050, 1150, 1250, and 1350K respectively. These thresholds are used to find the LOL in this work.

For the reactions  $C_{12}H_{25}O_2 \rightarrow C_{12}OOH-T6$ ,  $C_{12}OOHO_2 \rightarrow C_{12}KET-T6 + OH$ , and  $N-C_{12}H_{26} + HO_2 \rightarrow C_{12}H_{25} + H_2O_2$ , the LOL is shorter than the baseline mechanism as shown in Figure 4.7. This corroborates the previous findings in this study, as a short lift-off length is generally indicative of increased reactivity [53 and 54].  $C_{12}H_{25}O_2 \rightarrow C_{12}H_{24} + HO_2$  is not shown in the figure as it did not combust during the simulation time provided. The mechanisms that contained the modified  $CH_3 + HO_2 \leftrightarrow CH_3O + OH$  and  $H + O_2 \leftrightarrow O + OH$  reactions had similar lift-off lengths to that of the baseline mechanism. As discussed in [11], the reactions that are related to the first stage ignition processes show a direct relation to the stabilized LOL. The LOL from each mechanism is compared to experimental data in Figure 4.7.

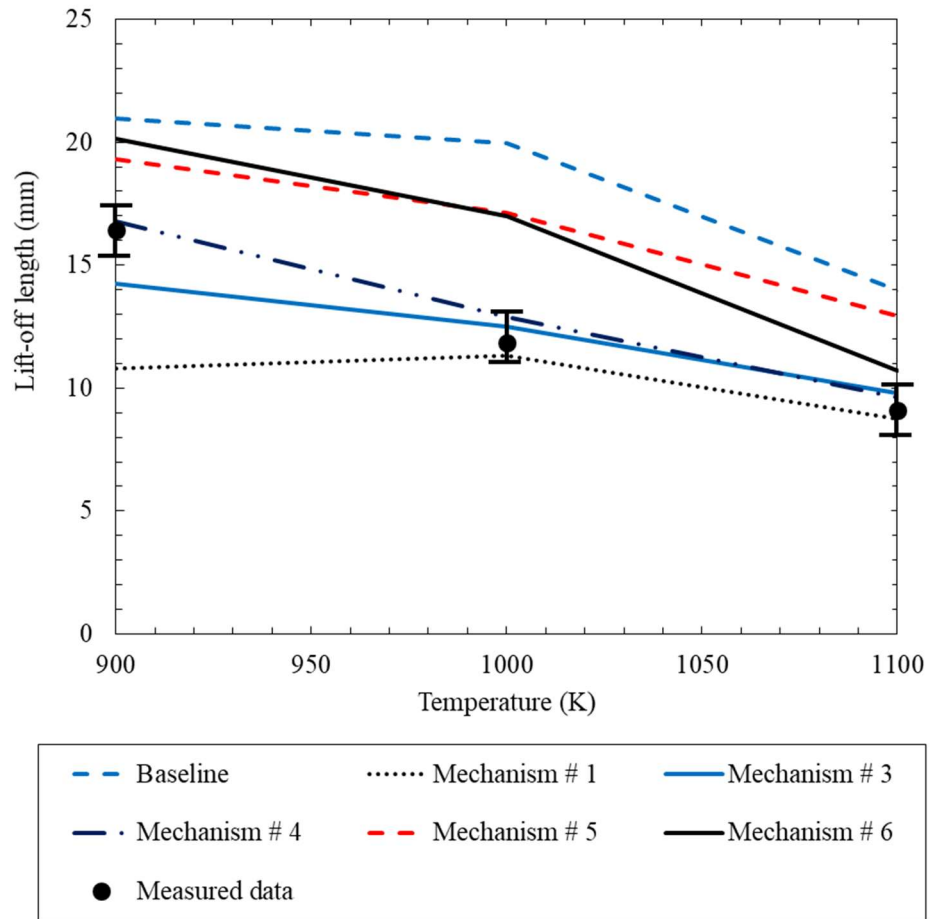


Figure 4.7 Flame lift-off lengths for each mechanism compared to experimental data of [1].

## Chapter 5

### 5 Conclusion

Combustion of n-dodecane was simulated in a constant volume batch reactor (0-D) and through turbulent spray (3-D) in a combustion chamber. A reduced chemical mechanism was used for the combustion modelling. A sensitivity analysis was performed to identify the reactions that are most important to the ignition delay timing; six reactions were identified. The reaction rates of these reactions were independently modified and used in individual mechanisms to study their impact on the ignition delay. Thus, six new mechanisms were built, in which one reaction per mechanism was changed. These mechanisms were subjected to 0-D and 3-D ignition delay simulations, in which the results were compared with experimental data.

None of the mechanisms (including the original one) could accurately predict low temperature combustion (a temperature range of 750 to 850 K) during the batch reactor simulations (0-D) due to the deficiency of the chemical pathways at low-temperature combustion. Thus, only turbulent spray combustion of n-dodecane at gas temperatures of 900, 1000, and 1100 K were simulated.

Ignition delays of all the mechanisms were compared to observe the effect of the reaction rates on the ignition delay. The mechanism with the unmodified reaction is called baseline, which all the new mechanisms were compared to for the 0-D and 3-D simulations. The difference between the baseline and the modified mechanisms were not of the same degree for the 0-D and the 3-D simulations at the studied conditions. While some differences between the two types of simulations are small, as is the case for the  $\text{CH}_3 + \text{HO}_2 \leftrightarrow \text{CH}_3\text{O} + \text{OH}$  at gas temperature of 1000 K, some cases had a significant disparity between the two simulation types. This was the case for the reaction  $\text{C}_{12}\text{H}_{25}\text{O}_2 \rightarrow \text{C}_{12}\text{H}_{24} + \text{HO}_2$  at 1100 K as the 0-D model predicted minimal changes but the 3-D model predicted a difference that was greater than two orders of magnitude from the

baseline mechanism. This is puzzling as turbulence chemistry interaction was not modelled for spray simulation, implying that chemistry should be the driving factor for both simulation types. This could be caused by how spray combustion occurs. Temperature gradients caused by the difference in the initial fuel and ambient gas temperature subjugates the fuel to a minimum temperature of approximately 600 K for the studied cases (the fuel temperature is 373 K for these cases). The rate at which the fuel reaches the critical reaction temperature (i.e. when the fuel ignites) is dependent on how the quickly the fuel disperses and absorbs thermal energy. This implies that the process of ignition between 0-D and 3-D simulations are not a direct nor suitable comparison of mechanism validation.

Flame lift-off length (LOL) was simulated to determine how the modified reaction rates affect the LOL. The modified reactions that significantly decrease the ignition delay time ( $C_{12}H_{25}O_2 \rightarrow C_{12}OOH-T6$ ,  $C_{12}OOHO_2 \rightarrow C_{12}KET-T6 + OH$ , and  $N-C_{12}H_{26} + HO_2 \rightarrow C_{12}H_{25} + H_2O_2$ ), also decrease the LOL. The mechanism with the reaction  $CH_3 + HO_2 \leftrightarrow CH_3O + OH$  showed a negligible impact on the LOL for all tested temperatures except 1100 K. At this initial gas temperature, the LOL increased. Similarly, the mechanism with the modified  $H + O_2 \leftrightarrow O + OH$  reaction increases the lift-off length for all initial ambient gas temperatures despite decreasing the ignition delay. These results indicate that the lift-off length is more dependent to initial ignition reactions as shown through the following reactions:  $C_{12}H_{25}O_2 \rightarrow C_{12}OOH-T6$ ,  $C_{12}OOHO_2 \rightarrow C_{12}KET-T6 + OH$ , and  $N-C_{12}H_{26} + HO_2 \rightarrow C_{12}H_{25} + H_2O_2$ . In addition, these reactions that affect the initial ignition delay in the baseline mechanism are not fully developed. The reactions that greatly reduce the ignition delay (i.e.  $C_{12}H_{25}O_2 \rightarrow C_{12}OOH-T6$ ,  $C_{12}OOHO_2 \rightarrow C_{12}KET-T6 + OH$ , and  $N-C_{12}H_{26} + HO_2 \rightarrow C_{12}H_{25} + H_2O_2$ ) reduce the lift-off length and make it more in-line with measured data. This implies one of the following: either the primary combustion reactions have



errors within them that impede their predictions of the lift-off length or there is a different sub-model that impacts the lift-off length prediction to a degree large enough to reduce the LOL by 5 mm. This requires further evaluation.

The fuel liquid and vapor penetration lengths were simulated for each mechanism at all of the test conditions. All of the liquid penetration lengths reach the same approximate steady state value, as expected. However, mechanisms with a modified reaction rate that increased the reactivity of the fuel showed a decrease in n-dodecane (fuel) vapor penetration length, once the flame was fully developed. This is especially prevalent for the modified  $C_{12}H_{25}O_2 \rightarrow C_{12}OOH$ -T6,  $C_{12}OOHO_2 \rightarrow C_{12}KET$ -T6 +OH, and  $N-C_{12}H_{26} + HO_2 \rightarrow C_{12}H_{25} + H_2O_2$  reactions, as the temporally-averaged steady-state fuel vapor penetration lengths are approximately 15, 17, and 18 mm, respectively. Juxtaposed, the baseline mechanism simulated an averaged vapor penetration length of 25 mm at the steady-state condition. The mechanism that did not have combustion occur (i.e. the mechanism with the modified  $C_{12}H_{25}O_2 \rightarrow C_{12}H_{24} + HO_2$  reaction), showed a vapor penetration length that kept dispersing further into the combustion chamber. In short, reactions that increases the reactivity of the combustion (i.e. reactions that decreased the ignition delay) has shorter fuel vapor penetration lengths.

As a conclusion, it is insufficient to only validate a chemical mechanism using ignition delay times. Errors in a reactions' rate can drastically impact the ignition delay of turbulent spray combustion especially at higher gas temperatures as exemplified in this study. It may appear that a mechanism predicts ignition delay is within the experimental uncertainty when performing a 0-D ignition delay study. However, if a critical reaction has a minute error (<10%) associated with it (as amplified with the  $C_{12}H_{25}O_2 \rightarrow C_{12}H_{24} + HO_2$  reaction in this study), there can be critical errors (>100%) in the predictive ability of the mechanism when testing a 3-D combustion

simulation. Therefore, it is recommended that critical species (for n-dodecane,  $C_{12}H_{25}O_2$  and  $C_{12}H_{24}$  based on this study) have their time histories validated as well to improve the combustion performance.

## References

- [1] Engine Combustion Network <http://www.sandia.gov/ecn/>.
- [2] Naber, Jeffrey D. and Siebers, Dennis L. “Effects of Gas Density and Vaporization on Penetration and Dispersion of Diesel Sprays.” *SAE Technical Paper 960034* (1996).
- [3] Siebers, Dennis L. “Liquid-Phase Penetration in Diesel Sprays.” *SAE Technical Paper 980809* (1998).
- [4] Pickett, Lyle M., Kook, Sanghoon, and Williams, Timothy C. “Visualization of Diesel Spray Penetration, Cool-Flame, Ignition, High-Temperature Combustion, and Soot Formation Using High-Speed Imaging.” *SAE International Journal of Engines* Vol. 2 No. 1 (2009) 439–459.
- [5] Pickett, Lyle M., Kook, Sanghoon, and Williams, Timothy C. “Transient Liquid Penetration of Early-Injection Diesel Sprays.” *SAE Technical Paper 2009-01-0839* (2009).
- [6] Pickett, Lyle M., Manin, Julien, Genzale, Caroline L., Siebers, Dennis, L., Musculus, Mark P. B., and Idicheria, Cherian A. “Relationship Between Diesel Fuel Spray Vapor Penetration/Dispersion and Local Fuel Mixture Fraction.” *SAE International Journal of Engines* Vol. 4 No. 1 (2011) 764–799.
- [7] Manin, Julien, Bardi, Michele, Pickett, Lyle M., Dahms, Rainer, N., and Oefelein, Joseph C. “Microscopic investigation of the atomization and mixing processes of diesel sprays injected into high pressure and temperature environments.” *Fuel* Vol. 134 No. 15 (2014) 531–543.
- [8] Siebers, Dennis L. “Scaling Liquid-Phase Fuel Penetration in Diesel Sprays Based on Mixing-Limited Vaporization” *SAE Technical Paper 1999-01-0528* (1999).
- [9] Higgins, Brian, Siebers, Dennis, and Aradi, Allen. “Diesel-Spray Ignition and Premixed-Burn Behavior.” *SAE Technical Paper 2000-01-0940* (2000).
- [10] Higgins, Brian and Siebers, Dennis. “Measurement of the Flame Lift-Off Location on DI Diesel Sprays Using OH Chemiluminescence.” *SAE Technical Paper 2001-01-0918* (2001).

- [11] Pickett, Lyle M., Siebers, Dennis L., and Idicheria, Cherian A. "Relationship Between Ignition Processes and the Lift-Off Length of Diesel Fuel Jets." *SAE Technical Paper 2005-01-3843* (2005).
- [12] Benajes, Jesús, Payri, Raúl, Bardi, Michele, and Martí-Aldaraví, Pedro. "Experimental characterization of diesel ignition and lift-off length using a single-hole ECN injector." *Applied Thermal Engineering* Vol. 58 No. 1–2 (2013) 554–563.
- [13] Payri, Raúl, Viera, Juan P., Pei, Yuanjiang, and Som, Sibendu. "Experimental and numerical study of lift-off length and ignition delay of a two-component diesel surrogate." *Fuel* Vol. 158 (2014) 957–967.
- [14] Espey, Christoph, Dec, John E., Litzinger, Thomas A., and Santavicca, Domenic A. "Planar Laser Rayleigh Scattering for Quantitative Vapor-Fuel Imaging in a Diesel Jet." *Combustion and Flame* Vol. 109 (1997) 65-86.
- [15] Fielding, Joseph, Frank, Jonathan H., Kaiser, Sebastian A., Smooke, Mitchell D., and Long, Marshall B. "Polarized/Depolarized Rayleigh Scattering for Determining Fuel Concentrations in Flames." *Proceedings of the Combustion Institute* Vol. 29 (2002) 2703–2709.
- [16] Idicheria, Cherian A. and Pickett, Lyle M. "Quantitative Mixing Measurements in a Vaporizing Diesel Spray by Rayleigh Imaging." *SAE Technical Paper 2007-01-0647* (2007).
- [17] Blessinger, Matthew, Meijer, Maarten, Pickett, Lyle M., Manin, Julien, and Skeen, Scott. "Quantitative Mixing Measurements and Stochastic Variability of a Vaporizing Gasoline Direct- Injection Spray." *8<sup>th</sup> U.S. National Combustion Meeting*. 070HE-0114. Salt Lake City, Utah, May 19-22, 2013.

- [18] Desantes, Jose M., Payri, Raul, Pastor, Jose M., and Gimeno, Jaime. "Experimental Characterization of Internal Nozzle Flow and Diesel Spray Behavior. Part I: Nonevaporative Conditions." *Atomization and Sprays* Vol. 15 No. 5 (2005) 489–516.
- [19] Payri, Raul, Salvador, F. Javier, Gimeno, Jaime, and De la Morena, Joaquin. "Effects of nozzle geometry on direct injection diesel engine combustion process." *Applied Thermal Engineering* Vol. 29 No. 10 (2009) 2051–2060.
- [20] Golovitchev, Valeri I., Nordin, Norathirah, Jarnicki, R., and Chomiak, Jerzy. "3-D Diesel Spray Simulations Using a New Detailed Chemistry Turbulent Combustion Model." *SAE Technical Paper 2000-01-1891* (2000).
- [21] Wright, Yuri M., Margari, Ourania-Nektaria, Boulouchos, Konstantinos, De Paola, Giorgio, and Mastorakos, Epaminondas. "Experiments and Simulations of n-Heptane Spray Auto-Ignition in a Closed Combustion Chamber at Diesel Engine Conditions." *Flow Turbulence Combustion* Vol. 84 No. 1 (2010) 49–78.
- [22] Luo, Zhaoyu, Som, Sibendu, Sarathy, S. Mani, Plomer, Max, Pitz, William J., Longman, Douglas E. and Lu, Tianfeng. "Development and validation of an n-dodecane skeletal mechanism for spray combustion applications." *Combustion Theory and Modelling* Vol. 18 No. 2 (2014) 187–203.
- [23] Samimi Abianeh, Omid, Curtis, Nicholas, and Sung, Chih-Jen. "Determination of modeled luminosity-based and pressure-based ignition delay times of turbulent spray combustion." *International Journal of Heat and Mass Transfer* Vol. 103 (2016) 1297–1312
- [24] Samimi Abianeh, Omid, Chen, Chien-Pei and Mahalingam, Shankar. "Modeling of Multi-Component Droplet Coalescence in Evaporating and Non-Evaporating Diesel Fuel Sprays." *International Journal of Automotive Technology* Vol. 15 No. 7 (2014) 1091–1100.

- [25] Ra, Youngchul and Reitz, Rolf D. "A vaporization model for discrete multi-component fuel sprays." *International Journal of Multiphase Flow* Vol. 35 No. 2 (2009) 101–117.
- [26] Samimi Abianeh, Omid, Chen, Chien-Pei, and Mahalingam, Shankar. "Numerical modeling of multi-component fuel spray evaporation process." *International Journal of Heat and Mass Transfer* Vol. 69 (2014) 44–53.
- [27] Kärholm, Fabian P., Tao, Feng, and Nordin, Niklas. "Three-Dimensional Simulation of Diesel Spray Ignition and Flame Lift-Off using OpenFOAM and KIVA-3V CFD Codes." *SAE Technical Paper 2008-01-0961* (2008)
- [28] Som, Sibendu, Longman, Douglas E., Luo, Zhaoyu, Plomer, Max, Lu, Tianfeng, Senecal, Peter K., and Pomraning, Eric. "Simulating Flame Lift-Off Characteristics of Diesel and Biodiesel Fuels Using Detailed Chemical-Kinetic Mechanisms and LES Turbulence Model." *ASME Internal Combustion Engine Division Fall Technical Conference*. ICEF2011-60051. Morgantown, WV, October 2-5, 2011
- [29] Venugopal, Rishikesh and Abraham, John. "A Numerical Investigation of Flame Lift-Off in Diesel Jets." *Combustion Science and Technology* Vol. 179 (2007) 2599–2618.
- [30] Som, Sibendu, Senecal, Peter K., and Pomraning, Eric. "Comparison of RANS and LES Turbulence Models against Constant Volume Diesel Experiments." *24<sup>th</sup> Annual Conference on Liquid Atomization and Spray Systems*. San Antonio, TX, May 20-23, 2012.
- [31] Hori, Tsukasa, Senda, Jiro, Kuge, Takahiro, and Fujimoto, H. Gen. "Large Eddy Simulation of Non-Evaporative Diesel Spray in Constant Volume Vessel by Use of KIVALES." *SAE Paper 2006-01-3334* (2006)
- [32] ANSYS Chemkin Theory Manual 17.0 (15151), Reaction Design: San Diego, 2015.

- [33] Smith, J. M., Van Ness, H. C., and Abbott, M. M. *Introduction to Chemical Engineering Thermodynamics*. McGraw-Hill, New York (2005).
- [34] Turns, Stephen R. *An Introduction to Combustion: Concepts and Applications*. McGraw-Hill, New York (2011)
- [35] Bedford, K.W. and Yeo, W.K., "Conjunctive Filtering Procedures in Surface Water Flow and Transport," *Large Eddy Simulation of Complex Engineering and Geophysical Flows*. St Petersburg Beach, FL, December 19-21 1993.
- [36] Pomraning, Eric. "Development of Large Eddy Simulation Turbulence Models." PhD Thesis. University of Wisconsin-Madison, Madison, WI, 2000.
- [37] Goyal, Ashraya. "Turbulent Spray Combustion Modeling Using Direct Integration Of Chemistry And Flamelet Generated Manifolds." Master Thesis. Wayne State University, Detroit, MI, 2017.
- [38] Issa, Raad. "Solution of the Implicitly Discretised Fluid Flow Equations by Operator-Splitting," *Journal of Computational Physics*. Vol. 62 No. 1 (1986) 40-65
- [39] Reitz, Rolf and Diwakar, R. "Structure of High-Pressure Fuel Sprays," *SAE Technical Paper 870598* (1987)
- [40] Reitz, Rolf. Computer Modeling of Sprays. *Spray Technology Short Course*, Pittsburgh, PA, 1996.
- [41] Reitz, Rolf D. "Modeling Atomization Processes in High-Pressure Vaporizing Sprays," *Atomisation and Spray Technology* Vol. 3 No. 4 (1987) 309-337
- [42] Kong, Song-Chang, Han, Zhiyu, and Reitz, Rolf D., "The Development and Application of a Diesel Ignition and Combustion Model for Multidimensional Engine Simulation," *SAE Technical Paper 950278* (1995)

- [43] Richards, K. J., Senecal, P. K., and Pomraning E., CONVERGE (Version 2.3) Manual, Convergent Science, Inc., Middleton, WI, 2016.
- [44] Xin, Jun, Ricart, L., and Reitz, R.D., "Computer Modeling of Diesel Spray Atomization and Combustion." *Combustion Science and Technology* Vol. 137 No. 1-6 (1998) 171-194
- [45] Schmidt, David P. and Rutland, C.J. "A New Droplet Collision Algorithm," *Journal of Computational Physics* Vol. 164 No. 1 (2000) 62-80
- [46] Post, Scott L. and Abraham, John. "Modeling the Outcome of Drop-Drop Collisions in Diesel Sprays." *International Journal of Multiphase Flow* Vol. 28 No. 6 (2002) 997-1019
- [47] Hou, Shuhai. "Investigation of the Interaction Mechanisms Between Closely Spaced Sprays From Micro-Hole Nozzles," Ph.D. Thesis. University of Massachusetts Amherst, Amherst, MA, 2005.
- [48] Ashgriz, N. and Poo, J.Y., "Coalescence and Separation in Binary Collisions of Liquid Drops." *Journal of Fluid Mechanics* Vol. 221 (1990) 183-204.
- [49] Manuel, A., Gonzalez, D., Borman, Gary, and Reitz, Rolf. "A Study of Diesel Cold Starting using both Cycle Analysis and Multidimensional Calculations," *SAE Technical Paper 910180* (1991)
- [50] Amsden, Anthony A., O'Rourke, Peter J., and Butler, T. Daniel. "KIVA-II: A Computer Program for Chemically Reactive Flows with Sprays." Technical Report No. LA-11560-MS. Los Alamos National Laboratory, Los Alamos, NM. 1989.
- [51] Narayanaswamy, Krithika, Pepiot, Perrine, and Pitsch, Heinz. "A chemical mechanism for low to high temperature oxidation of n-dodecane as a component of transportation fuel surrogates." *Combustion and Flame*. Vol 161. No. 4 (2014): pp: 866-884.



[52] Samimi Abianeh, Omid and Bravo, Luis. "A comparison study of predicted pressure-based ignition delay time of n-dodecane fuel using various skeletal kinetic mechanisms." *46<sup>th</sup> AIAA Fluid Dynamics Conference*. AIAA 2016-3961. Washington, D.C., June 13-17, 2016.

[53] Payri, Raul, Garcia-Oliver, Jose M., Bardi, Michele, and Manin, Julien. "Fuel temperature influence on diesel sprays in inert and reacting conditions." *Applied Thermal Engineering* Vol. 35 No. 1 (2012) pp: 185-195.

[54] Shen, His-Peng S., Steinberg, Justin, Vanderover, Jeremy, and Oehlschlaeger, Matthew A. "A shock tube study of the ignition of n-heptane, n-decane, n-dodecane, and n-tetradecane at elevated pressures." *Energy & Fuels* Vol. 23 No. 5 (2009) pp: 2482-2489.

**ABSTRACT****UNCERTAINTY IN COMBUSTION REACTION RATES AND ITS EFFECTS ON  
COMBUSTION SIMULATIONS**

by

**JOSHUA PIEHL****May 2018****Advisor:** Dr. Omid Samimi-Abianeh**Major:** Mechanical Engineering**Degree:** Master of Science

This work investigates the uncertainties in reaction rates of an n-dodecane model on turbulent spray combustion simulations. Six major reactions were found to significantly impact the ignition delay of the mechanism in a 0-D batch reactor model. These reactions' rates were independently modified and placed into individual mechanisms. These newly developed mechanisms were simulated in a 3-D turbulent spray simulation and a 0-D batch reactor at a pressure of 60 bar and temperatures from 900 to 1100 K. The combustion characteristics (e.g. ignition delays, flame lift-off length, liquid and vapor penetration) of the modified mechanisms were compared to those produced by the original mechanism. The impact of the reaction on the ignition delay timing was different between the 0-D and 3-D simulations, with an average difference of 30%. This indicates that kinetic mechanism validation through ignition delay timing alone is insufficient.

## **AUTOBIOGRAPHICAL STATEMENT**

I was born in Detroit on December 31, 1992. Growing up in southeast Michigan, I have always been fascinated with the automotive industry. However, I was concerned about the damage the automotive industry was doing to the environment. Climate change has always been a big concern of mine, as I was raised to be environmentally conscious. After I graduated from high school, I decided I wanted to become an engineer, appealing to my automotive interests while promoting environmental awareness.

I completed my Bachelor's degree in mechanical engineering at Lawrence Technological University in Southfield, Michigan. It was here that I became attracted to combustion physics and renewable energy. After graduation, I began working in the automotive industry at Fiat Chrysler Automobiles. Simultaneously, I enrolled for my Master's degree at Wayne State University. After working in the industry for some time, I returned to school full time and began performing combustion research where I believed I could do the most good. During my time at Wayne State, I have researched combustion speciation of different fuels numerically and experimentally. My findings have produced the work I have made today in addition to some on-going projects. I am continuing my education to obtain my Ph.D. in mechanical engineering at Wayne State. Professionally, I would like to continue researching combustion physics to mitigate the impact internal combustion engines have on the environment until the world transitions away from fossil fuels.